3-23-2023

Numerical Modeling of Caldera Formation Using Smoothed Particle Hydrodynamics (SPH)

Benjamin Mullet
Stanford University

Paul Segall
Stanford University

Alomir Favero
ahf009@bucknell.edu

submitted to *Geophys. J. Int.*

Numerical modeling of caldera formation using Smoothed Particle Hydrodynamics (SPH)

B. Mullet[1⋆], P. Segall[1], A. H. Fávero Neto[2]

[1]*Department of Geophysics, Stanford University*

[2]*Department of Civil & Environmental Engineering, Bucknell University*

Received 29 March 2023

SUMMARY

Calderas are kilometer-scale basins formed when magma is rapidly removed from shallow magma storage zones. Despite extensive previous research, many questions remain about how host rock material properties influence the development of caldera structures. We employ a mesh-free, continuum numerical method, Smoothed Particle Hydrodynamics (SPH) to study caldera formation, with a focus on the role of host rock material properties. SPH provides several advantages over previous numerical approaches (finite element or discrete element methods), naturally accommodating strain localization and large deformations while employing well-known constitutive models. A continuum elastoplastic constitutive model with a simple Drucker-Prager yield condition can explain many observations from analogue sandbox models of caldera development. For this loading configuration, shear band orientation is primarily controlled by the angle of dilation. Evolving shear band orientation, as commonly observed in analogue experiments, requires a constitutive model where frictional strength and dilatancy decrease with strain, approaching a state of zero volumetric strain rate. This constitutive model also explains recorded loads on the down-going trapdoor in analogue experiments. Our results, combined with theoretical scaling arguments, raise questions about the use of analogue models to study caldera formation. Finally, we apply the model to the 2018 caldera collapse at Kīlauea volcano and conclude that the host rock at Kīlauea must exhibit relatively low dilatancy to explain the inferred near-vertical ring faults.

Key words: Calderas – Numerical modeling – Geomechanics

1 INTRODUCTION

Volcanic calderas are kilometer-scale surface depressions, round in shape, that are formed when overlying material collapses into a depleted melt storage zone as the result of an eruption (Acocella, 2021; Branney & Acocella, 2015). While often associated with extremely large explosive eruptions that produce hundreds to thousands of cubic kilometers of erupted material (Smith & Bailey, 1968; Hildreth & Mahood, 1986; Jellinek & DePaolo, 2003; Gregg, De Silva, Grosfils, & Parmigiani, 2012), calderas have also formed during eruptions of more modest size (1 km^3 or less) and intensity (Francis, 1974; Branney & Acocella, 2015). Similarly, a range of magma types are associated with caldera formation (Cashman & Giordano, 2014). Large silicic calderas are formed in explosive eruptions where magma erupts along caldera ring faults; basaltic calderas (e.g., Figure 1) are generally formed as magma is laterally withdrawn from a reservoir and migrates to a remote vent or dike (Acocella, 2021). Nevertheless, many questions remain about what factors control the initiation and orientation of the ring faults that bound calderas.

Both analogue and numerical models have provided valuable insights into caldera development (Geyer & Martí, 2014). These experiments demonstrate that caldera development is controlled by factors such as the strength of the rock and geometric factors (Acocella, 2007, 2021). For example, the ratio of the depth of magma chamber to the width of the chamber (H/B in Figure 2) has been shown to significantly influence the surface deformation. For sufficiently shallow chambers, caldera collapse occurs as a coherent block moves down along reverse faults; for deeper chambers multiple faults interact to accommodate more complex deformation (Roche, Druitt, & Merle, 2000). Other experiments have studied the significant role of regional or tectonic stresses

⋆ bmullet@stanford.edu

in caldera formation. In particular, extensional stresses may lead to favorable conditions for dike propagation and ring fault development (Gudmundsson, 2006; Cabaniss, Gregg, & Grosfils, 2018).

Analogue models generally employ sand as the scaled representation of rock and generate deformation by manipulating a scaled "magma chamber" (Figure 2). To construct analogue models, not only must the geometry of the system be faithfully scaled, but stresses (including those induced by body forces) and constitutive behavior must be considered as well (Hubbert, 1937). One goal of this paper is to consider the scaling of the analogue problem and show that while it may be possible to scale many elements of the caldera forming systems, it is exceedingly difficult to scale all elements appropriately. We refer to both theory (Section 3) and the results of numerical models (Section 5), and show that certain aspects of sand's constitutive behavior – primarily, its significant dilatancy and critical state behavior – might not be appropriate analogues for the in situ behavior of rock.

The simplest analogue model of caldera formation is equivalent to the classic "trapdoor problem" from soil mechanics (Terzaghi, 1936) (Figure 2), in which a trapdoor is lowered beneath a box of soil, typically sand. (Note that the term "trapdoor" has also been used to refer to a characteristic style of asymmetric caldera development (Lipman, 1997), which is not the focus of this paper.) In the geotechnical and soil mechanics literature, the trapdoor problem has been explored to study soil "stress arching," in which the vertical stress on the trapdoor decreases dramatically with small displacements of the trapdoor due to stress transfer to the box on either side of the trapdoor (Costa, Zornberg, Bueno, & Costa, 2009; Iglesia, Einstein, & Whitman, 2014; Terzaghi, 1943). This problem is relevant for many geotechnical engineering problems, such as the settlement of piles and the stresses exerted on underground pipes. Here we make extensive use of the results of Chevalier, Combe, and Villard (2012), a stress arching study from the geotechnical literature. This study offers a unique perspective into the trapdoor problem, as it reports the vertical load exerted on the trapdoor, as a function of trapdoor displacement.

Most previous numerical research on caldera development employs one of two numerical methods: the Finite Element Method (FEM) (Gudmundsson, 2007; Gregg et al., 2012; Kabele, Žák, & Somr, 2017) or Discrete Element Method (DEM) (Hardy, 2008; Holohan, Schöpfer, &

Walsh, 2011, 2015). While both of these techniques have yielded valuable insights about caldera formation, both techniques have limitations. FEM is an extremely well established and widely used technique, and, as a continuum method, conveniently allows for familiar continuum constitutive models. Nevertheless, as a mesh-based method, FEM struggles to naturally adapt to large deformations and strain localization, both of which are intrinsic to caldera formation. DEM models, on the other hand, offer a discrete, mesh-free option, naturally accommodating large deformations and strain localization (e.g., Holohan et al., 2011). However, as a fully discrete method, a user must fine tune inter-particle forces to approximate a continuum constitutive model (Cundall & Strack, 1979). These inter-particle forces may have natural interpretations for granular media such as sand, but it is unclear how to best scale these forces to the caldera scale. Furthermore, because appropriate use of DEM can require the simulation of millions or billions of particles, the computational demand of DEM models can be impractical (Bui, Sako, & Fukagawa, 2006).

Here we employ a numerical method, Smoothed Particle Hydrodynamics (SPH), which is particularly well suited to the study of caldera formation. SPH solves the *continuum* problem over a collection of *mesh-free* particles. As SPH is a continuum method, we can employ common elastoplastic constitutive models and easily interpret the results in terms of continuum stresses and strains. As a mesh-free method, large deformations and shear localization are naturally accommodated, while keeping computational costs relatively low.

SPH, a technique originally developed in the late 1970s for astrophysical problems (Gingold & Monaghan, 1977; Lucy, 1977), has since seen wide application in a variety of disciplines. Indeed, one of the first authors to propose the SPH technique, Joseph Monaghan, later published two papers on caldera development (Gray & Monaghan, 2003, 2004), although this work was limited to studying incipient host rock failure due to *increased* pressure in a magma chamber. Recently, SPH has been more widely applied to both geomechanics and the simulation of granular media (Bui & Nguyen, 2021; Fávero Neto & Borja, 2018; Fávero Neto, Askarinejad, Springman, & Borja, 2020). In this work we employ `GEOSPH`, a SPH code originally developed in del Castillo, Fávero Neto, and Borja (2021b, 2021a), who used the method to explore several classical geomechanics problems. This paper builds on these earlier works by presenting a shear-weakening constitutive model (approximating critical state behavior) and using SPH to study caldera formation.

As a framing for the content of this paper, we refer to the 2018 eruption of Kīlauea volcano (Figure 1). This eruption represents a spectacular recent example of caldera development and is the best-instrumented example of caldera collapse on record (Neal et al., 2019; Anderson et al., 2019). Over the course of several months, over one cubic kilometer of lava erupted along Kīlauea's East Rift Zone (Neal et al., 2019). As magma was withdrawn from the summit, Kīlauea caldera was significantly enlarged as portions of the caldera floor descended up to five hundred meters along both pre-existing and newly developed ring faults.

Here, we explore how the material properties of the Kīlauea host rock exert control over the orientation of the ring faults that formed in the eastern sector of the caldera during the 2018 eruption. While these faults are inward-dipping and normal at the surface, both geodetic (Segall, Anderson, Johanson, & Miklius, 2019; Segall, Anderson, Pulvirenti, Wang, & Johanson, 2020) and seismic (Shelly & Thelen, 2019) evidence indicate that these ring faults are vertical or near-vertical at depth. (While basaltic caldera collapses are known to be episodic, occurring in short duration Very Long Period (VLP) seismic events, stable creep may also contribute to collapse.) This finding stands in contrast to the results of analogue models, which often find that early deformation in caldera formation is accommodated along outward dipping thrust faults (Acocella, 2007). In this paper, we reconcile these two observations, and show that the dip of ring faults is primarily controlled by the dilatancy of the host rock. We conclude that the dilatancy of the host rock at Kīlauea must be fairly low to explain the observed ring fault orientation at depth.

The primary objective of this paper is to explore what factors control the development of caldera structures, with a particular emphasis on material properties and constitutive models. In this pursuit, we first discuss the trapdoor problem (Section 2). We then present theoretical arguments to establish what scaled analogue models can – and cannot – tell us about the caldera formation problem (Section 3). Next, we provide the details of the SPH method, and discuss the strain-weakening constitutive model that we employ that mimics critical state behavior for dense sands (Section 4). In the Results (Section 5), we show that our numerical method can adequately

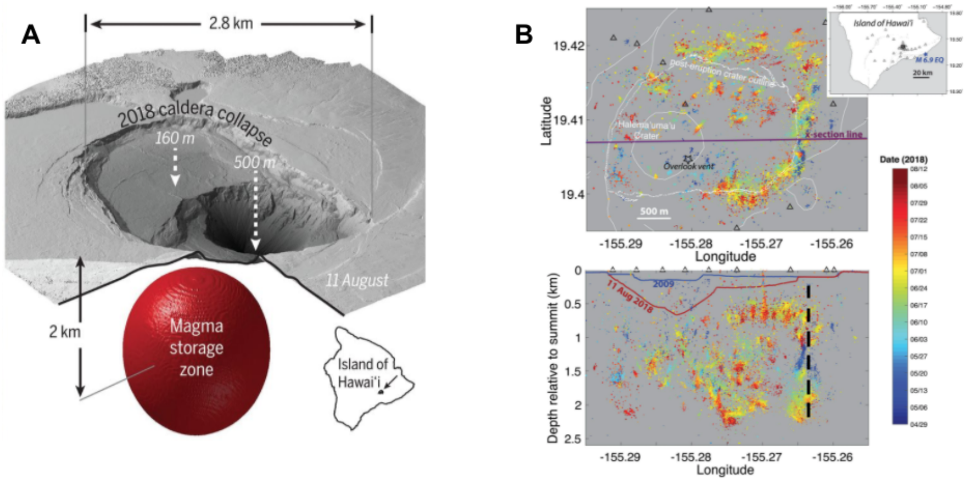

Figure 1. Observations from the 2018 caldera collapse event at Kīlauea volcano. (A) Digital elevation model highlighting areas of dramatic subsidence and location of inferred magma storage zone based on modeling of pre-collapse deformation (from Anderson et al., 2019). (B) Seismic locations indicate vertically-oriented ring faults (from Shelly & Thelen, 2019, dashed line has been added to denote vertical fault structure, color indicates time).

explain both the kinematics and the load transfer observed in trapdoor experiments, but only by adopting a constitutive model with critical state behavior. We also show that the near-vertical ring faults observed during the 2018 Kīlauea collapse demand a relatively low-dilatancy host rock. In the Discussion (Section 6), we consider the implications of these results for the use of continuum constitutive models and appropriate construction of analogue experiments.

2 A SIMPLE MODEL OF CALDERA COLLAPSE: THE TRAPDOOR PROBLEM

In this paper we study the simplest model of caldera formation, the 2-D (plane strain) version of the "trapdoor problem" from soil mechanics (Figure 2). A box of width L and height H is filled with a granular material. A trapdoor of width B is then slowly lowered (to study active arching) or raised (to study passive arching). Here, we limit our analysis to the case where the trapdoor is lowered, which mimics caldera collapse. Note that the trapdoor motion imparts a *displacement* boundary condition, while in an actual caldera with a depleting reservoir, a *stress* boundary condition might be more appropriate. We reserve the treatment of different boundary conditions for future work.

Stress arching is usually observed in trapdoor models (Terzaghi, 1936), reflecting the elasto-

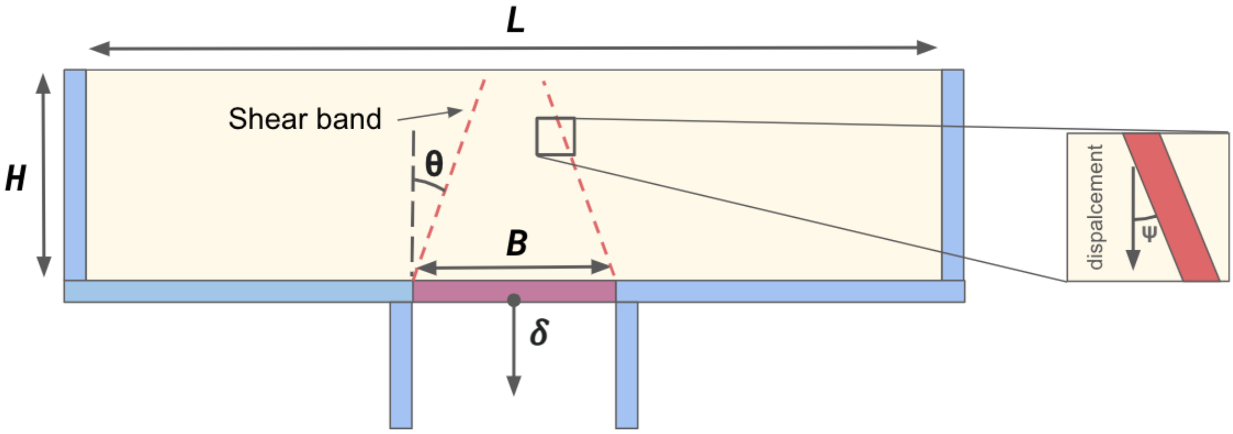

Figure 2. Schematic of the "trapdoor problem," an idealized model of caldera formation. Soil (depth H, width L) is contained within rigid boundaries. The center piece of the bottom boundary (the "trapdoor") is moved downward with specified displacement $\delta(t)$. "Stress arching" and development of shear bands then occurs. The angle between the shear bands and vertical is θ. The angle of dilation ψ forms the angle between the relative displacement and the direction of a shear band.

plastic behavior of sand. Before the trapdoor is lowered, the vertical load exerted on the trapdoor is equal to the weight of the overlying sand, $\rho g H$, where ρ is the density of the sand, g is the acceleration due to gravity, and H is the depth of the sand. Over a small initial displacement of the trapdoor, the deformation is accommodated in an elastic fashion. In this phase a stress arch initially forms, which allows for part of the vertical load that had been exerted on the trapdoor to be transferred to the experimental apparatus at the boundary of the trapdoor. As a result, the vertical load on the trapdoor decreases. As deformation continues, the stress along the stress arch increases to the point of plastic failure. Plastic strains then accumulate in shear bands that originate at the corners of the trapdoor (Figure 2). These shear bands are observable in many trapdoor and analogue caldera formation experiments via observations using techniques such as Particle Image Velocimetry (PIV) (Ruch, Acocella, Geshi, Nobile, & Corbi, 2012). These shear bands are interpreted as the equivalent of faults in natural caldera systems.

Here we use the parameter θ, which is defined as the angle between the shear band and the vertical, to denote the orientation of the shear bands (Figure 2). As noted previously (Costa et al., 2009), for a simple Drucker-Prager constitutive model (which shares many essential elements with the Mohr-Coulomb model, details in Section 4), the angle θ should be largely controlled by the angle of dilation, which we denote ψ. This follows from the basic geometric interpretation of the angle of dilation (Figure 2), which quantifies the angle between a shear band and the direction of motion of the soil mass adjacent to the shear band (Davis & Selvadurai, 2005). (Note that the only way for this angle to be a value greater than zero is by allowing the soil to increase in volume, hence the name "dilation" angle.) In this paper we will present numerical results which confirm that the orientation of shear bands is primarily controlled by the angle of dilation.

The constitutive model for sands that we have adopted in this paper, a non-associative Drucker-Prager model (described in detail below), has a yield surface defined by a cohesion c and angle of internal friction ϕ. (These parameters have the same essential meaning as in the more common Mohr-Coulomb model.) We discuss this constitutive model in depth in Section 4, but here note the connection between the angle of dilation ψ and the angle of friction ϕ. To satisfy the condition of non-negative plastic work, the angle of friction must always be greater than the angle of dilation (Borja, 2013). In the case of sand, a physical intuition for this requirement can be derived by considering the two sources of strength of the sand: First, the frictional resistance generated as two grains slide past each other, and, second, the resistance caused by the interlocking nature of grains. In order for two grains to move past each other, they must first overcome this interlocking. In other words, the sand must first dilate to allow for plastic flow. Thus we can see the connection between the angle of dilation and the angle of friction: the angle of friction accounts for both the resistance due to interlocking (the angle of dilation) and an additional frictional resistance.

It is commonly observed in analogue models of caldera formation that the initially outward-dipping shear bands which bound the down-going parcel of sand rotate to become more vertical (or even inward-dipping) as the displacement of the trapdoor increases (Chevalier et al., 2012; Ruch et al., 2012). We propose that this change in shear band orientation is due to a changing value of the angle of dilation as plastic strain accrues. This idea aligns with a "critical state" model of sand behavior (Jefferies, 1993), where sands undergoing shear dilate (or contract) until a critical density (porosity) is reached. Intuitively, this concept agrees with the interpretation of the angle of dilation as quantifying the interlocking of sand particles; after a certain finite amount of dilation, grains no longer are interlocked and therefore interlocking will no longer influence the strength or the volumetric deformation of the sand. There are many critical state constitutive models that have been developed for a variety of soils (Roscoe & Burland, 1968; Jefferies, 1993; Wood, 1990). Here, we use a strain-softening constitutive model that mimics the critical state behavior of dense sands (Section 4). This model allows for the reduction of the angle of friction and angle of dilation with increasing plastic deformation, eventually reaching a "critical state" of zero volumetric strain rate. In this way, the constitutive model we employ is not a proper critical state model that would allow for both compaction and dilation, but does provide a simple approximation of the critical state behavior of dense sands that dilate under deformation until a critical state is achieved. We therefore refer to the model as a "simplified critical state" model. We find that this simple model satisfactorily explains the kinematics and forces observed in trapdoor experiments.

3 SCALING OF ANALOGUE CALDERA MODELS

The proper scaling of analogue models is a topic that has received considerable attention (Hubbert, 1937; Panien, Schreurs, & Pfiffner, 2006; Ramberg, 1981). Here we provide some insights relevant to caldera formation.

Assuming geometric scaling has been satisfied (that is, all relevant lengths are in the same proportion in the lab scale and caldera scale), the scaling of stresses (or forces) remains. Assuming that accelerations are small enough to be negligible, the stresses must follow quasi-static equilibrium,

$$\nabla \cdot \boldsymbol{\sigma} = \rho g \hat{\boldsymbol{z}}, \tag{1}$$

where $\boldsymbol{\sigma}$ is stress and $\hat{\boldsymbol{z}}$ is the unit vector pointing in the positive z direction (up). Note that by using Equation 1 we restrict our attention to experiments which are conducted at rest on Earth's surface; while some trapdoor experiments have been conducted using centrifuges (Costa et al., 2009; Iglesia et al., 2014), the vast majority of caldera formation analogue experiments are conducted under ambient gravity.

Non-dimensionalization leads to

$$\nabla^* \cdot \boldsymbol{\sigma}^* = \left(\frac{\rho_0 g H}{\sigma_c}\right) \rho^* \hat{\boldsymbol{z}}, \tag{2}$$

where ρ_0 is the characteristic density, H is the depth of the sand (our choice for a characteristic length), and σ_c is a characteristic stress. Asterisks denote non-dimensional variables.

In order for an analogue model to be properly scaled, the non-dimensional quantity in parentheses in Equation 2 must be the same for the Earth scale and the lab-scale model. This non-dimensional number quantifies the balance between gravitational (body) forces and stresses. It is straightforward to assign values to ρ_0 and H at both scales, and we assume g is constant. The issue is thus how to properly set the value of σ_c, the characteristic stress.

Before we discuss this choice, it is useful to first establish the necessary ratio between the characteristic stress at the field and lab scales. We take ρ_0 and H to be 2900 kg/m^3 and 1000 m, respectively, in the field scale, numbers that are representative of the basaltic caldera at Kīlauea (Anderson et al., 2019); for a sandbox model we take the values 1800 kg/m^3 for ρ_0 and 5 cm for H. Thus the quantity $\rho_0 g H$ is 3.2×10^4 times greater in the field case than in the lab case. In order for the the non-dimensional ratio in Equation 2 to stay constant, the ratio of σ_c in the field and lab should also scale by 3.2×10^4.

There are multiple potential choices for σ_c. For a Drucker-Prager (or Mohr-Coulomb) yield condition, the plastic yield stress is determined by the combined influence of the cohesion and the angle of friction. We can thus propose two potential values of σ_c: (1) c, the cohesion, or (2) $\rho_0 g H \tan(\phi)$, a characteristic frictional stress equal to the the lithostatic load at the bottom of the sandbox times the coefficient of friction. Both of these values need to be scaled appropriately.

Thus the cohesion of the material in the sandbox model needs to be a factor of $\sim 3.2 \times 10^4$ less than the cohesion of rock. If we take a rock cohesion of 3 MPa, a value that is appropriate for a partially fractured basaltic rock mass (Schultz, 1993), we therefore require a sand cohesion of ~ 90 Pa, which is within the range of cohesion claimed by some modelers by adding crushed silica powder to sand (Ruch et al., 2012; Norini & Acocella, 2011).

Scaling using the frictional stress leads to the conclusion that the angle of internal friction ϕ needs to be constant between the two scales. Although the angle of friction is generally greater in rock than sand (Andersen & Schjetne, 2013; Carmichael, 1982), this requirement should also be tractable.

Thus appropriately scaling plastic yield stress of an analogue model should be possible. What about the elastic response? Most authors choose to ignore this part of the deformation (e.g. Norini & Acocella, 2011) because plastic strains are assumed to be much larger than elastic strains (Ramberg, 1981). While this is undoubtedly true for tectonic-scale processes that take place over millions of years, it is less clear that elastic deformation can be ignored in smaller length- and time-scale processes such as caldera collapse, particularly in the early stages of deformation, when shear bands (faults) have not fully developed. To answer this question, in this section we perform a scaling argument that compares the accumulated elastic strains to the accumulated plastic strains. In Section 5 we perform numerical tests to verify the utility of these scaling relations.

In an elastoplastic constitutive model, the elastic stress is in effect capped by the plastic yield function. Assuming that in the case of the trapdoor problem plastic failure first develops near the trapdoor where lithostatic loads are relatively high, we can ignore the effect of cohesion and say that the plastic yield surface is defined by a characteristic frictional stress $\rho g H \tan(\phi)$. This stress can therefore be used to set a characteristic value for the elastic strain ε_e at plastic failure.

On the other hand, after yielding commences, plastic strains continue to accrue without limitation. Assuming plastic strains are large, we can say that the plastic strain is thus approximately the total strain. We therefore define the characteristic plastic strain ε_p as

$$\varepsilon_p = \frac{\delta}{H}. \tag{3}$$

Comparing the characteristic elastic and plastic strains we can define a non-dimensional number which we call the elastoplastic regime number, Λ_{ep},

$$\Lambda_{ep} \equiv \frac{G\delta}{\rho g H^2 \tan(\phi)}. \tag{4}$$

When Λ_{ep} is large, we expect plastic strains to dominate; when it is small, we expect elastic strains to be non-negligible. For the Kīlauea example from before, we took ρ_0 and H to be 2900 kg/m^3 and 1000 m, respectively. Taking ϕ to be 30°, δ to be 500 m, and the elastic shear modulus of the host rock, G, to be 10 GPa gives a value of Λ_{ep} of about 300, indicating that, by the end of the caldera collapse, elastic strains are probably negligible. Nevertheless, at earlier stages of caldera development (up until $\delta \sim 20$ meters), Λ_{ep} is less than or equal to 10, such that elastic strains might not be negligible. However, experiments are needed to determine over which ranges of Λ_{ep} different regimes of behavior are observed. We provide results from numerical experiments to help constrain possible ranges in Section 5.

Note that thus far, we have limited our discussion to the caldera scale context. For properly building a scaled model, we also need to consider the laboratory sandbox scale model.

If scaling of elastic parameters is needed, challenges arise. To scale elastic constitutive behavior in a linearly elastic model we need to scale two elastic moduli. Assuming that the Poisson's ratio of rock and sand is approximately the same, we can reduce this problem to scaling the shear modulus, G. Using the scaling conversion from earlier and assuming a shear modulus of rock around 10 GPa, we would thus need a shear modulus of sand around 10 GPa / (3.2×10^4) = 0.3 MPa. Given that the static shear modulus of dense sand is likely 50 - 100 MPa (Hardin, 1965), this requirement is problematic.

If we revisit our earlier scaling, we could design an analogue model where the scaling of elastic moduli would result in a sand shear modulus in a range of tractable values. However, it is exceedingly difficult to scale *both* the shear modulus and cohesion appropriately, at the same time. Shear moduli in rock are 100 - 200 times greater than shear moduli in sand; cohesions are 50,000 times greater in rock (or more) than sand and crushed silica mixtures.

Even if these constitutive parameters are appropriately scaled, however, there remains one fundamental assumption that is difficult to verify: that a single continuum constitutive model can explain both the deformation of the host rock in a real caldera and the deformation of sand in a analogue model. Due to its granular nature the deformation of sand is extremely complex, and the search for satisfactory continuum constitutive models for sands is an ongoing area of research (Forterre & Pouliquen, 2008; Jop, Forterre, & Pouliquen, 2006; GDR MiDi, 2004; Roux & Combe, 2002). On the other hand, caldera host rock might be heavily jointed or horizontally layered, leading to complex continuum behavior (Gudmundsson, 2007).

Here we take it as given that the constitutive behavior of sand and rock can both be described using continuum elastoplastic constitutive models. However, we do not assume that both sand and rock can be described by the *same* constitutive model. In subsequent sections we show that a simplified critical state constitutive model – which allows for initial dilation followed by zero volumetric strain rate at large deformations – is necessary to explain the results from a simple sandbox analogue model. This leads to important considerations for the use of scaled analogue models, because this critical state behavior must be scaled appropriately in order to ensure valid results.

4 MODELING CALDERA FORMATION USING SMOOTHED PARTICLE HYDRODYNAMICS

4.1 The SPH method

The SPH method is a continuum collocation method (a variant of the method of weighted residuals, MWR) where displacement and stress tensors are calculated at the same locations (co-location) in the computational domain. The idea in a MWR is to minimize the residual error in the approximation of a partial differential equation (PDE) solution in a weighted sense. More specifically, in the collocational variant, the minimization of the weighted residual is imposed on N sample points (henceforth denoted *particles*), which serve as both mathematical points (where the PDE solution is found) and Lagrangian representative volumes of matter (i.e., that they do not represent individual physical particles of sand or rock). Hence, what we want to achieve in the SPH method ideally is

$$\int_{\Omega} W(\mathbf{x}-\mathbf{x}_i, h)\mathbf{r}(\mathbf{x})d\mathbf{x} = 0\,, \tag{5}$$

such that

$$\mathbf{r}\left(\mathbf{x}_i\right) = \mathbf{0},\ i = 1, 2, ..., N\,, \tag{6}$$

where $\boldsymbol{r}(\mathbf{x})$ is the vector of residuals corresponding to the PDE of the problem (detailed below), $W(\mathbf{x}-\mathbf{x}_i)$ is the weighting function, h is a length scale, and $\boldsymbol{x}$ is the vector representing the position of a particle in the problem domain Ω.

In SPH, the weighting function is a smooth function called the kernel function (or kernel). The kernel should satisfy a number of conditions, among which the most important are: (1) symmetry (evenness), (2) positivity, (3) compact support, and (4) unity property. For more details on the

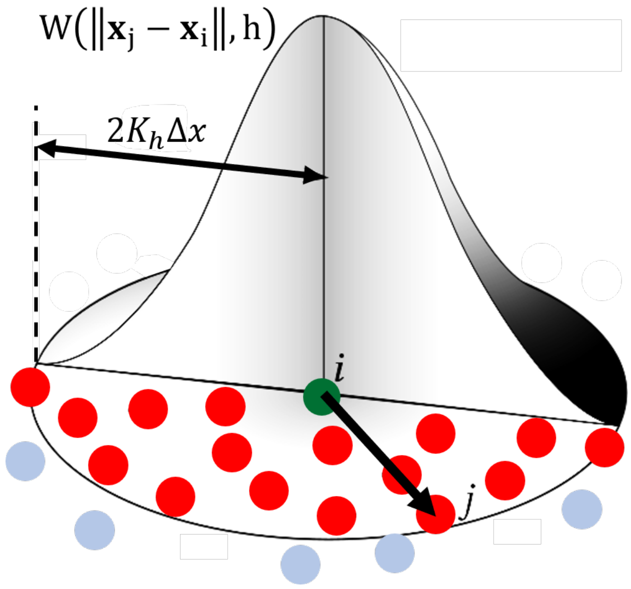

Figure 3. The SPH kernel function allows for a discretization of the continuum equations via discrete particles.

kernel and its properties, the reader is referred to Liu and Liu (2010). The most commonly used kernels in practice resemble bell-shaped curves like the one shown in Figure 3.

Referring to Figure 3 we can see that the length scale h defines the size (radius) of the compact support of the kernel, and in SPH is called *smoothing length*. The particle at which the kernel is centered is denoted particle "i," and any other surrounding particles within the kernel support are denoted generically using the subscript "j," and are called neighbor particles. The smoothing length is a function of the initial interparticle distance (Δx), such that $h = K_h \Delta x$, with $1.0 < K_h < 2.0$ a constant. The radius of the kernel then is sh, and as shown in Figure 3, $s \approx 2.0$ (also a constant). Hence, the kernel evaluates to zero everywhere outside its support and only neighbor particles within the kernel of particle i will influence it. The most common kernels used in practice are the cubic spline kernel (Monaghan & Lattanzio, 1991) and the Wendland C2 kernel (Wendland, 1995). In this work, we use the Wendland C2 kernel.

The mechanical problem that we are interested in solving is represented by an initial boundary value problem (IBVP), stated as follows

For a domain Ω with boundary $\partial\Omega$ such that $\overline{\Omega} = \Omega \cup \partial\Omega$, $\partial\Omega = \partial\Omega_v \cup \partial\Omega_h$, and $\partial\Omega_v \cap \partial\Omega_h = \emptyset$, given $\boldsymbol{g} : \Omega \rightarrow \mathbb{R}^3$, $\overline{\boldsymbol{v}} : \partial\Omega_v \rightarrow \mathbb{R}^3$, and $\boldsymbol{b} : \partial\Omega_h \rightarrow \mathbb{R}^3$, find $\boldsymbol{u} : \overline{\Omega} \rightarrow \mathbb{R}^3$ such that:

$$\frac{1}{\rho}\nabla \cdot \boldsymbol{\sigma} + \mathrm{g} = \boldsymbol{a} \quad \text{in } \overline{\Omega} \times t \tag{7}$$

$$\frac{d\rho}{dt} = \rho \nabla \cdot \boldsymbol{v} \quad \text{in } \overline{\Omega} \times t \tag{8}$$

$$\boldsymbol{v} = \overline{\boldsymbol{v}} \quad \text{on } \partial\Omega_v \times t \tag{9}$$

$$\boldsymbol{\sigma} \cdot \mathbf{n} = \boldsymbol{b} \quad \text{on } \partial\Omega_h \times t \tag{10}$$

Subject to initial conditions $\boldsymbol{u} = \boldsymbol{u}_0$, $\boldsymbol{v} = \boldsymbol{v}_0$, $\boldsymbol{a} = \boldsymbol{a}_0$, $\boldsymbol{b} = \boldsymbol{b}_0$, and $\boldsymbol{\sigma} = \boldsymbol{\sigma}_0$ at $t = 0$.

Here, $\boldsymbol{\sigma}$ is the Cauchy stress tensor, "$\nabla\cdot$" is the divergence operator with respect to the spatial configuration, ρ is the current mass density, g is the vector of body force per unit mass (herein, gravity), vectors $\boldsymbol{v}$ and $\boldsymbol{a}$ are the particle velocity and acceleration, $\mathbf{n}$ is the unit vector normal to boundary $\partial\Omega_h$, $\overline{\boldsymbol{v}}$ and $\boldsymbol{b}$ are the vectors of prescribed velocities and tractions, and t is time. Equations 7 and 8 represent the balance of linear momentum and of mass, respectively.

We can discretize Equation 7 in the SPH formalism to illustrate the procedure. The first step of deriving SPH operators is to make use of Equation 5 where the residual version of Equation 7 is defined as

$$\boldsymbol{r}(\mathbf{x}) = \nabla \cdot \boldsymbol{\sigma} + \rho(\boldsymbol{g} - \boldsymbol{a}) \tag{11}$$

Substituting Equation 11 into 5, and defining $W_i = W(\mathbf{x} - \mathbf{x}_i, h)$ yields

$$\int_\Omega W_i \left[\nabla \cdot \boldsymbol{\sigma} + \rho(\boldsymbol{g} - \boldsymbol{a})\right] d\mathbf{x} = \int_\Omega W_i \nabla \cdot \boldsymbol{\sigma} d\mathbf{x} + \int_\Omega W_i \rho(\mathbf{g} - \boldsymbol{a})\, d\mathbf{x} = \mathbf{0}\,. \tag{12}$$

Using the divergence theorem, we can rewrite Equation 12 as

$$\int_{\partial\Omega} W_i \boldsymbol{\sigma} \cdot \mathbf{n} d\mathbf{x} - \int_\Omega \nabla \otimes W_i \cdot \boldsymbol{\sigma} d\mathbf{x} + \int_\Omega W_i \rho(\mathbf{g} - \boldsymbol{a})\, d\mathbf{x} = \mathbf{0}\,, \tag{13}$$

where $\nabla\otimes = d/d\mathbf{x}$, is the gradient operator.

Using the compact support property of the kernel, for an internal particle, the first integral above is equal to zero, and hence

$$-\int_\Omega \nabla \otimes W_i \cdot \boldsymbol{\sigma} d\mathbf{x} + \int_\Omega W_i \rho(\mathbf{g} - \boldsymbol{a})\, d\mathbf{x} = \mathbf{0}\,, \tag{14}$$

Note that for particles near the domain boundary, the surface integral in Equation 13 will not vanish. This will require some corrections to the operators and the kernel gradient. We briefly discuss the latter in Appendix A.

The first integral in Equation 14 is referred to in SPH literature as the kernel approximation of the divergence of a field variable, and the second integral is an example of the kernel approximation of a field variable.

The next step in deriving the SPH operators is the defining characteristic of the SPH method. In this step, the integrals in Equation 14 are transformed into summations over each particle, which in SPH literature is called *particle approximation* (or *summation approximation*). Using a simple trapezoidal rule to perform the numerical integration of a function in $\mathbb{R}^3$, we first define the integration volume associated with a set of discrete points in the integration domain $\mathbf{x}_j$ $(j = 1, 2, ..., N)$, defined as

$$V_j = \frac{m_j}{\rho_j}\,, \tag{15}$$

where $m_j = m(\mathbf{x}_j)$ and $\rho_j = \rho(\mathbf{x}_j)$ are the mass, and mass density at each point j, respectively.

Using this volume, the integrals in Equation 14 can be approximated as summations

$$\int_\Omega \nabla \otimes W_i \cdot \boldsymbol{\sigma} d\mathbf{x} \approx \sum_{j=1}^{N} \nabla \otimes W_{ji} \cdot \boldsymbol{\sigma}_j V_j\,, \tag{16}$$

$$\int_\Omega W_i \rho \left(\mathbf{g} - \boldsymbol{a}\right) d\mathbf{x} \approx \sum_{j=1}^{N} W_{ji} \rho_j \left(\mathbf{g}_j - \boldsymbol{a}_j\right) V_j\,, \tag{17}$$

where $\nabla \otimes W_{ji} = \left[\frac{dW_i(\mathbf{x})}{d\mathbf{x}}\right]_{\mathbf{x}=\mathbf{x}_j} = -\nabla \otimes W_{ij} = \left[\frac{dW_j(\mathbf{x})}{d\mathbf{x}}\right]_{\mathbf{x}=\mathbf{x}_i}$, and $W_{ij} = W_i(\mathbf{x}_j) = W_{ji}$. Note that we used the symmetry and evenness properties of the kernel to write the previous identities. Making use of the unit property of the kernel, the right-hand side of Equation 17 simplifies to $\rho_i \left(\mathbf{g}_i - \boldsymbol{a}_i\right)$, and hence, based on Equations 16 and 17, the basic discrete SPH operator for the balance of linear momentum can be written as

$$\langle \boldsymbol{a} \rangle_i = \frac{1}{\rho_i} \sum_{j=1}^{N} \nabla \otimes W_{ij} \cdot \boldsymbol{\sigma}_j V_j + \boldsymbol{g}_i\,, \tag{18}$$

where the $\langle\rangle$ brackets denote the SPH approximation of a field variable.

Many different versions of the SPH operators can be derived to possess desired properties. For further details, the reader is referred to Fávero Neto (2020) and Violeau (2012). The most commonly used SPH discrete operators for the dynamic balance of linear momentum and balance of mass (Bui & Nguyen, 2021), also used in this paper, are respectively,

$$\langle \boldsymbol{a} \rangle_i = \sum_{j=1}^{N} m_j \left(\frac{\boldsymbol{\sigma}_i + \boldsymbol{\sigma}_j}{\rho_i \rho_j} \right) \cdot \nabla \otimes W_{ij} + \boldsymbol{g}_i \,, \tag{19}$$

and

$$\dot{\rho}_i = \left\langle \frac{d\rho}{dt} \right\rangle_i = \sum_{j=1}^{N} m_j (\boldsymbol{v}_j - \boldsymbol{v}_i) \cdot \nabla \otimes W_{ij} \,. \tag{20}$$

In order to complete the purely mechanical SPH formulation we need to connect the state of stress of the material to the kinematics of motion (displacements and velocities). This is achieved through a constitutive law that relates deformation and stress (or strain rates and stress rates). In this work, the time rate of change Cauchy stress tensor, $\dot{\boldsymbol{\sigma}}$, is connected to the rate of deformation tensor through the following constitutive relationship

$$\breve{\boldsymbol{\sigma}} = \mathbb{C}^{\mathrm{ep}} : \boldsymbol{d} \,, \tag{21}$$

where $\breve{\boldsymbol{\sigma}}$ is the Jaumann stress rate, required to enforce objectivity of the stress rate under large deformations, and $\boldsymbol{d}$ is the deformation rate tensor. The Jaumann stress rate is defined as

$$\breve{\boldsymbol{\sigma}} = \dot{\boldsymbol{\sigma}} + \boldsymbol{\sigma} \cdot \boldsymbol{\omega} - \boldsymbol{\omega} \cdot \boldsymbol{\sigma} \,, \tag{22}$$

while the deformation rate tensor is given by

$$\boldsymbol{d} = \frac{1}{2} \left[\nabla \otimes \boldsymbol{v} + (\nabla \otimes \boldsymbol{v})^{\top} \right] \,, \tag{23}$$

and

$$\boldsymbol{\omega} = \frac{1}{2} \left[\nabla \otimes \boldsymbol{v} - (\nabla \otimes \boldsymbol{v})^{\top} \right] \,, \tag{24}$$

is the spin rate tensor. In SPH, the following operators are used to discretize the deformation rate and spin rate tensors respectively

$$\langle \boldsymbol{d} \rangle_i = \frac{1}{2} \left[\sum_{j=1}^{N} V_j (\boldsymbol{v}_j - \boldsymbol{v}_i) \otimes \nabla \otimes W_{ij} + \left(\sum_{j=1}^{N} V_j (\boldsymbol{v}_j - \boldsymbol{v}_i) \otimes \nabla \otimes W_{ij} \right)^{\top} \right] \,,$$

$$\langle \boldsymbol{\omega} \rangle_i = \frac{1}{2} \left[\sum_{j=1}^{N} V_j (\boldsymbol{v}_j - \boldsymbol{v}_i) \otimes \nabla \otimes W_{ij} - \left(\sum_{j=1}^{N} V_j (\boldsymbol{v}_j - \boldsymbol{v}_i) \otimes \nabla \otimes W_{ij} \right)^{\top} \right] \,.$$

In the next section we will provide more details on the simplified critical state constitutive model used in this paper and the elastoplastic tangent modulus.

4.2 Simplified critical state constitutive model

As presented in the previous section, the stress rate is connected to the rate of deformation tensor through the elastoplastic tangent modulus, $\boldsymbol{C}^{\mathrm{ep}}$, which is defined as (Borja, 2013)

$$\boldsymbol{C}^{\mathrm{ep}} = \boldsymbol{C}^{\mathrm{e}} - \frac{1}{\chi}\boldsymbol{C}^{\mathrm{e}} : \frac{\partial \mathcal{Q}}{\partial \boldsymbol{\sigma}} \otimes \frac{\partial \mathcal{F}}{\partial \boldsymbol{\sigma}} : \boldsymbol{C}^{\mathrm{e}} \,, \tag{25}$$

where $\boldsymbol{C}^{\mathrm{e}}$ is the elastic fourth-order tangent modulus of the material, $\mathcal{F}$ is the yield function, $\mathcal{Q}$ is the plastic potential function, and

$$\chi = \frac{\partial \mathcal{F}}{\partial \boldsymbol{\sigma}} : \boldsymbol{C}^{\mathrm{e}} : \frac{\partial \mathcal{Q}}{\partial \boldsymbol{\sigma}} \,. \tag{26}$$

The plastic potential function allows the direction of plastic flow to be distinct from that defined by the yield surface, enabling the so-called non-associative plasticity. Furthermore, the plastic deformation is proportional to the plastic potential through the following relationship

$$\dot{\boldsymbol{\varepsilon}}^{p} = -\dot{\lambda}\frac{\partial \mathcal{Q}}{\partial \boldsymbol{\sigma}} \tag{27}$$

where λ is the so-called plastic multiplier (or consistency parameter) which is a measure of the magnitude of plastic deformation.

In this paper we adopt a simple elastoplastic model with a Drucker-Prager yield criterion combined with a simplified critical state formulation which allows for the internal friction angle ϕ and angle of dilation ψ of the material to vary with plastic strain, approaching a steady state of zero volumetric strain rate. In this model, we assume linear isotropic elasticity such that when the material is deforming in the elastic regime, its response can be expressed solely as a function of constant bulk and shear moduli, K and G, respectively. Hence, the elastic tangent modulus tensor takes the form

$$\boldsymbol{C}^{\mathrm{e}} = K\mathbf{1} \otimes \mathbf{1} + 2G\left(\boldsymbol{I} - \frac{1}{3}\mathbf{1} \otimes \mathbf{1}\right) \,, \tag{28}$$

where $\boldsymbol{I}$ is the fourth-order symmetric identity tensor, and $\mathbf{1}$ is the second-order identity tensor.

The Drucker-Prager criterion is assumed to govern yielding of the material, and is expressed as

$$\mathcal{F}\left(I_1, J_2\right) = \sqrt{2J_2} + \alpha_\phi I_1 - k_c \leq 0\,, \tag{29}$$

where $J_2 = |\boldsymbol{S}|^2/2$ is the second invariant of the deviatoric part of the Cauchy stress tensor, $\boldsymbol{S}$, and $I_1 = \mathrm{tr}\left[\boldsymbol{\sigma}\right]$ is the first invariant of the Cauchy stress tensor. Parameters α_ϕ and k_c relate to the Mohr-Coulomb parameters of the material, ϕ and c (cohesion), respectively. For plane strain analyses, α_ϕ and k_c are given by (del Castillo et al., 2021b)

$$\alpha_\phi = \frac{\sqrt{2}\tan\phi}{\sqrt{9+12\tan^2\phi}} \quad \text{and} \quad k_c = \frac{3\sqrt{2}c}{\sqrt{9+12\tan^2\phi}}\,. \tag{30}$$

In Equation 25, when the yield and plastic potential functions are chosen to be the same, $\mathcal{F} = \mathcal{Q}$, we have so-called associative plasticity. However, for geotechnical and geological materials, a non-associative behavior is more common, i.e., $\mathcal{F} \neq \mathcal{Q}$. Hence, in this work, we assume a plastic potential function of the form (del Castillo et al., 2021a)

$$\mathcal{Q} = \sqrt{2J_2} + \alpha_\psi I_1\,, \tag{31}$$

where α_ψ depends on the angle of dilation of the material, ψ, through the following relationship for plane strain analyses (del Castillo et al., 2021b)

$$\alpha_\psi = \frac{\sqrt{2}\tan\psi}{\sqrt{9+12\tan^2\psi}}\,. \tag{32}$$

In order to model the critical state behavior of geological materials, we follow Zabala and Alonso (2011), and defined simple exponential functions relating the constitutive parameters to accumulated plastic strain, $\varepsilon_{\mathrm{p,acc}}$,

$$\phi = \phi_r + (\phi_0 - \phi_r)e^{-\varepsilon_{\mathrm{p,acc}}/\eta_c}, \tag{33}$$

$$\psi = \psi_0 e^{-\varepsilon_{\mathrm{p,acc}}/\eta_c}, \tag{34}$$

where ϕ_r is the residual friction angle, ϕ_0 and ψ_0 are the initial values for the friction angle and angle of dilation, respectively, and η_c quantifies the characteristic plastic strain over which ψ and ϕ decay. Note that in this formulation, ϕ asymptotically approaches ϕ_r while ψ asymptotically approaches zero. Moreover, note that despite its simplicity, the model used here also allows for strain softening through the reduction of the internal friction angle.

It should be noted that the simplified model given by Equations 33 and 34 is not a proper critical state model, because the evolution in material parameters is connected directly to strain and there is no well defined critical state void ratio (porosity). Nevertheless, we follow Bui and Nguyen (2021) in using the critical state terminology because the model allows for initial volume change followed by zero volumetric strain rate (zero dilation angle) at large deformations, a defining feature of critical state models.

For further information regarding the numerical implementation of the SPH method, please refer to Appendix A.

5 RESULTS

5.1 Kinematics of analogue models

Using constant values of ψ and ϕ (i.e., a non-critical state constitutive model), we first investigated the role of ϕ and ψ in controlling the kinematics of analogue models (Figure 4). The SPH model clearly captures shear banding in the sand that is well developed after 1 cm of trapdoor displacement. These shear bands originate at the trapdoor edges, matching the results of analogue experiments.

The orientation of shear bands (as measured by θ, Figure 2) stays relatively constant with increasing deformation. Our results further show that varying ψ leads to a a change in orientation, but changing ϕ while keeping ψ constant does not change the orientation of the shear bands.

The continuum stresses and strains produced by the SPH model make it simple to quantify this relationship between ψ and θ (Figure 5). We find that θ tracks with ψ across a broad range of values of ψ, and this result holds true whether ϕ is allowed to vary with ψ or is held constant. This agrees with the theoretical argument, outlined in the Introduction, that θ should equal ψ (Costa et al., 2009; Davis & Selvadurai, 2005).

5.2 Kinematics using simplified critical state constitutive model

With constant ψ, the value of θ stays relatively constant throughout the numerical experiments. This finding contrasts with what is normally observed in analogue experiments, where the orienta-

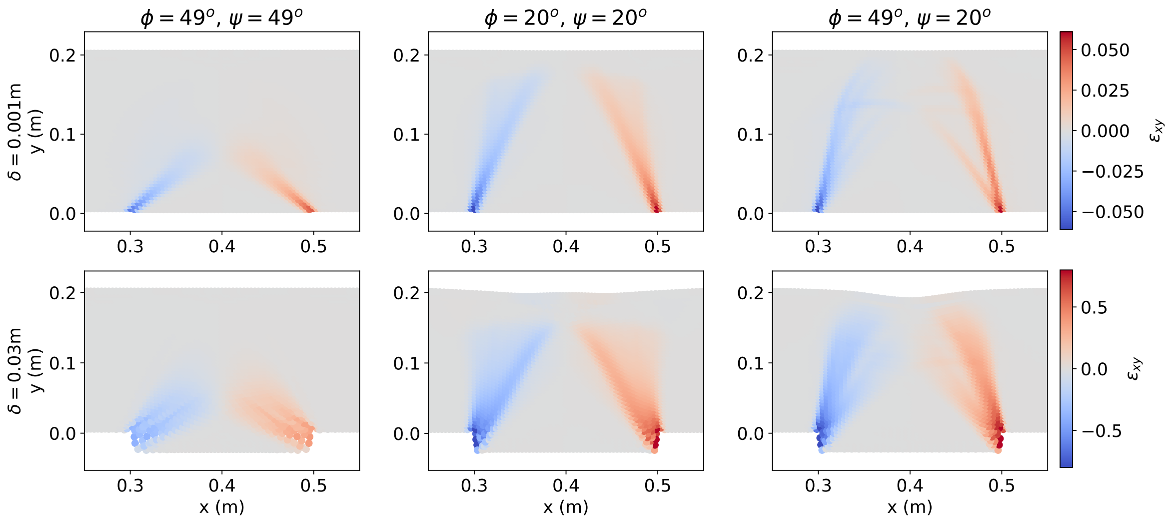

Figure 4. Shear strain in numerical sandbox models (constant ϕ and ψ). Each row is at the same displacement and shares a colorbar; each column has snapshots from one simulation with stated parameters. $H = 0.2$ m, $B = 0.2$ m, $c = 0$, $\Delta x = 0.004$ m.

tion of shear bands rotates to become more vertical with increasing trapdoor displacement (Ruch et al., 2012; Chevalier et al., 2012). We thus applied the simplified critical state constitutive model that allows for the value of ϕ and ψ to vary with plastic strain. As expected, the results from the

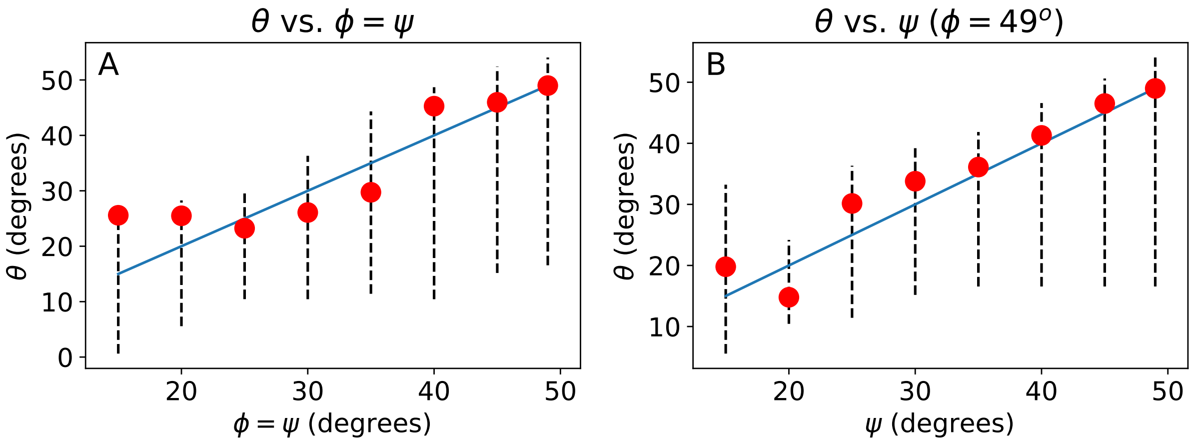

Figure 5. Orientation of shear band relative to vertical, θ (see Fig. 2), for models with different ϕ and ψ that are independent of deformation. Red dots represent the angle formed by best-fit line for the 20 particles with the greatest shear strain. Dashed lines denote extent of shearing region (25% of maximum shear strain). Solid blue line is $\theta = \psi$. (A) Associative (non-critical state) plastic flow, $\phi = \psi$. (B) Non-associative (non-critical state) plastic flow: constant ψ as in Figure 4 and $\phi = 49°$. Other parameters same as Figure 4.

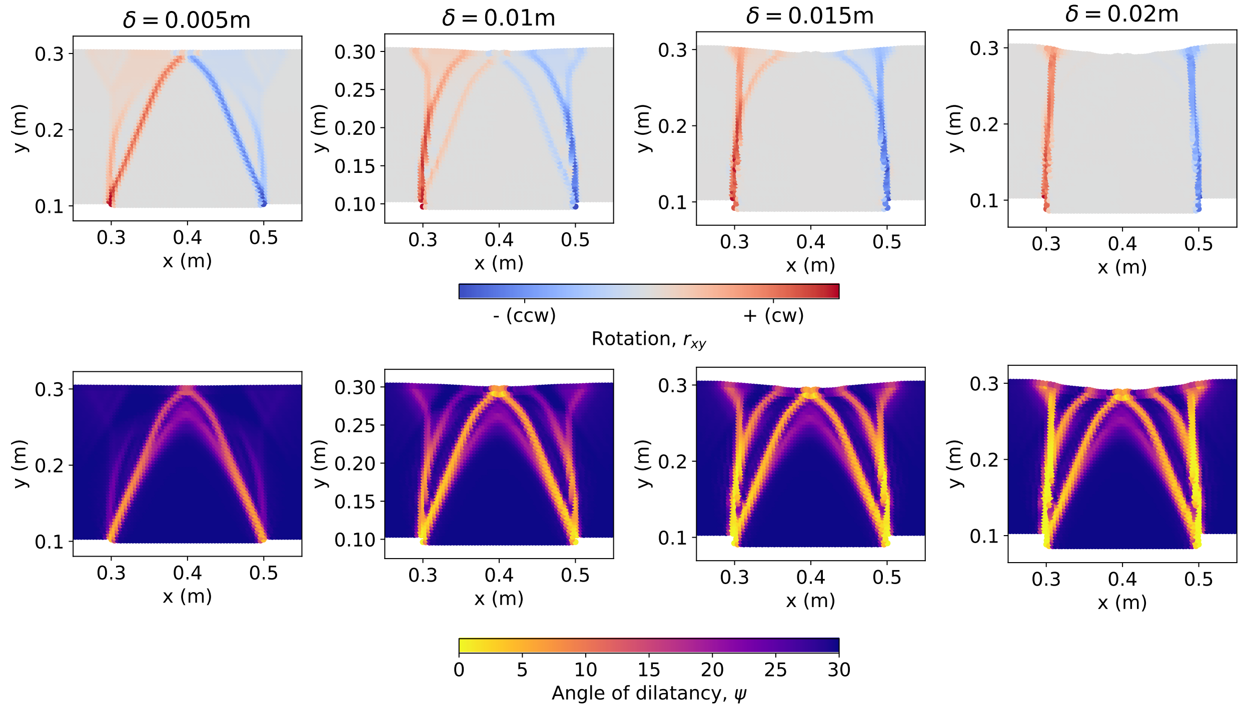

Figure 6. Top row: Rotation of particles for different trapdoor displacements, simplified critical state model (the xy component of the infinitesimal rotation tensor is plotted, similar to the observations reported by PIV studies, e.g. Ruch et al. (2012)). Counterclockwise (ccw) rotations are negative; clockwise (cw) rotations are positive. Bottom row: the angle of dilation, ψ, at the same trapdoor displacements as the top row. The angle of friction and the angle of dilation are calculated as a function of accumulated plastic strain (Equations 33 and 34). $H = 0.2$ m, $B = 0.2$ m, $c = 0$, $\Delta x = 0.004$ m, $\phi_0 = 49°$, $\phi_r = 15°$, $\psi_0 = 30°$, $\eta_c = 0.1$. Note that the top row reflects an instantaneous rate while the bottom row reflects a function of cumulative strain.

simplified critical state model demonstrate the target behavior of shear bands rotating to be more vertical with increasing trapdoor displacement (Figure 6).

With just a small amount of trapdoor displacement ($\delta = 0.5$ cm), shear strains have already localized sufficiently to cause plastic strain to accumulate and ψ to decrease towards zero within the shear bands. As the shear bands first localize at the boundary of the trapdoor, ψ decreases most quickly in the deeper part of the shear bands. This variation in ψ along the length of the shear band contributes to an increased curvature of shear bands as the trapdoor displacement increases.

Using our simplified critical state constitutive model, we attempted to explain the kinematics of the trapdoor experiment performed by Chevalier et al. (2012) (Figure 7). In order to fit the observed kinematics, we varied the constitutive parameters around the values reported in Chevalier

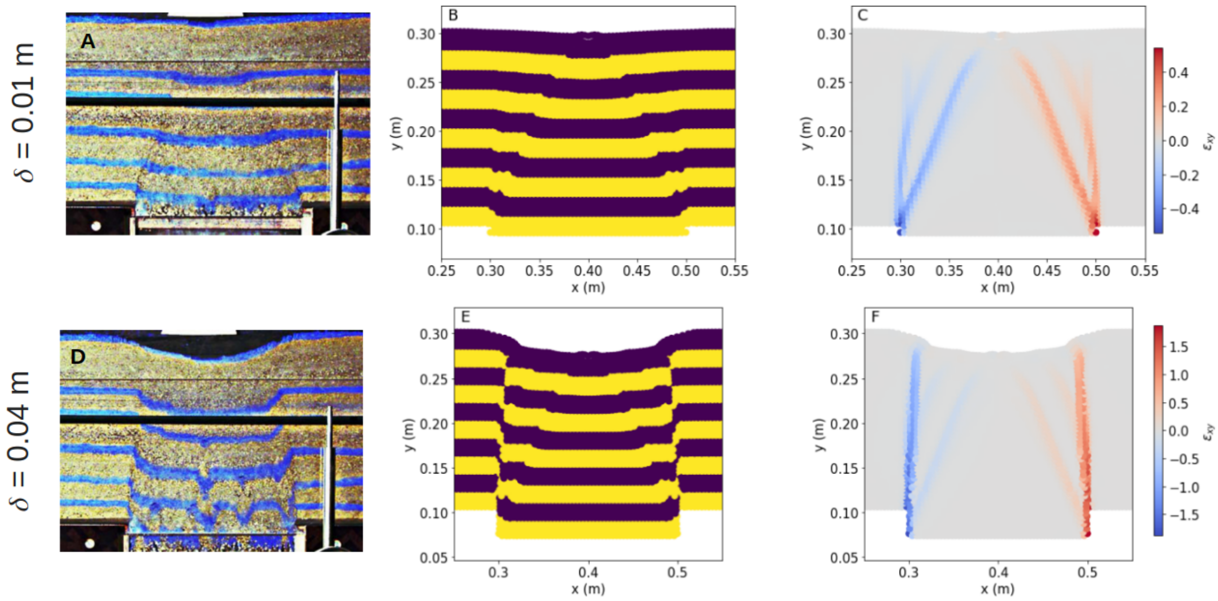

Figure 7. Kinematics of trapdoor model with simplified critical state plasticity matches the kinematics described in analogue sandbox models. Frames (A) and (D) are images taken from the analogue trapdoor experiments of Chevalier et al. (2012). Frames (B) and (E) are snapshots from SPH numerical experiments. In (A), (B), (D), and (E) color bands are to illustrate deformation only; material properties are uniform. Frames (C) and (F) show the accumulated shear strain at these displacements. Same material properties as in Figure 6.

et al. (2012), who reported a peak friction angle (ϕ_0) of $49°$, a residual friction angle (ϕ_r) of $39°$, and did not report a value for the dilation angle. We found we could satisfactorily reproduce the observed kinematics with an initial angle of dilation, $\psi_0 = 30°$, and a characteristic plastic strain, $\eta_c = 0.1$. The friction angle ϕ, and residual friction angle, ϕ_r, had a small effect on the kinematics, consistent with our earlier results (Figure 4).

In the Chevalier et al. (2012) experiments, early deformation ($\delta = 1$ cm) was isolated to a triangular-shaped wedge, bounded by straight, outwardly dipping thrust fault-like shear bands. Later deformation ($\delta = 4$ cm) transitioned to vertically-oriented shear bands. Our model produced qualitatively similar results (Figure 7 B, E) and demonstrated the transition from outwardly dipping to vertical shear bands (Figure 7 C, F).

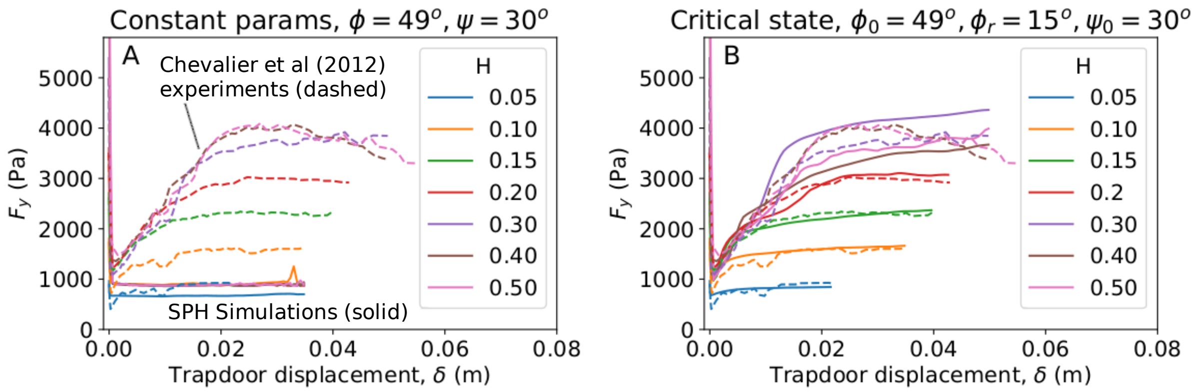

Figure 8. Load vs. displacement curves. Dashed lines represent the experimental values from Chevalier et al, 2012; solid lines are SPH results from this paper. Some $\delta = 0$ lithostatic loads are greater than the maximum F_y shown; axis is truncated to show detail for $\delta > 0$. (A) Constitutive model with constant values of ϕ and ψ is unable to fit the observed data. (B) A simplified critical state model that allows for ϕ and ψ to decrease with strain well explains the experimental data. Material properties not shown are the same as in Figure 6.

5.3 Load displacement curves

In addition to recording observations of the kinematics of the trapdoor problem, Chevalier et al. (2012) reported the vertical load exerted on the trapdoor. As with the kinematic observations, we attempted to fit the reported load displacement curves using both a constant parameter constitutive model and the simplified critical state constitutive model. As before, we found that the simplified critical state model was needed to explain the observations (Figure 8).

As identified by Chevalier et al. (2012), the experimental load displacement curves show three distinct phases. In the first (the "elastic phase") the vertical load on the trapdoor decreases dramatically as a stress arch develops. This phase lasts for only a very small ($\sim$ 1 mm) trapdoor displacement, before plastic yielding occurs. The second phase (the "transition phase") is defined by the vertical load being partially re-established on the trapdoor, and is apparent in the range 0.1 cm $< \delta <$ 2 cm, although the range varies depending on the sand depth. The transition phase is also defined by the rotation of shear bands to be more vertical. Finally, in the "critical phase," the load reaches a relatively constant value that does not change with δ. Note that this final load value depends on the original sand depth (Figure 8) for $H < 0.30$ m but is very similar for all experiments with $H \geq 0.30$ m. This likely reflects the influence of the non-dimensional parameter H/B, which has previously been shown to control the development of kinematic features of analogue models (Roche et al., 2000; Acocella, 2021).

These three phases are naturally explained by a critical state model. In the elastic phase, yielding has yet to occur. Once the transition phase begins, plastic deformation has begun, which causes the model to approach critical state (ϕ approaches ϕ_r and ψ approaches zero). Once enough plastic strain has developed, the model enters the critical phase.

Enforcing constant parameters (a non-critical state constitutive model), results in load displacement curves which do not exhibit a load recovery after the initial drop during the elastic phase (Figure 8 A). As the frictional strength and the orientation of the shear bands do not change, the mass of the parcel between the stress arch and trapdoor does not change; thus the load remains constant. A critical state model, on the other hand, allows for the orientation of the shear bands to change and the frictional resistance in the shear bands to decrease. This leads to an increase in the load exerted on the trapdoor (Figure 8 B).

The constitutive model parameters used to fit the load displacement curves (Figure 8) are the same as those used to fit the observed kinematics (Figure 7). This demonstrates the utility of the SPH method coupled with the simplified critical state constitutive model to explain both observed kinematics and forces.

5.4 The granular length scale

Our simplified critical state constitutive model includes the term η_c, which controls the rate at which critical state is approached (Equations 33 and 34). Up until this point we have treated this term as a fitting parameter, and varied its value in order to match the load displacement curves and kinematics reported by Chevalier et al. (2012) (Figures 7 and 8). However, the value of η_c can also be interpreted as indicating an intrinsic length scale, ℓ, for the problem.

The choice of η_c is related to the intrinsic length scale of the problem, which in turn is related to the smoothing length, h (Figure 9), in the simulations. By varying h, it can be seen that in order to approximately maintain the same model response, it is necessary to vary η_c according to the

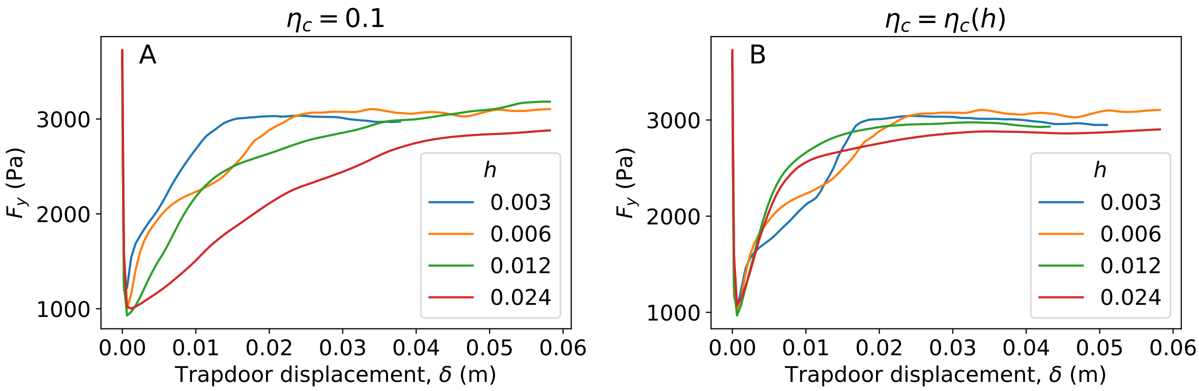

Figure 9. Load displacement curves for the $H = 0.2$ m case of the simplified critical state model in Figure 8, but with varied smoothing length, h. (A) Constant $\eta_c = 0.1$. (B) Variable $\eta_c = \ell/h$, with $\ell = 0.6$ mm.

equation

$$\eta_c = \frac{\ell}{h}, \tag{35}$$

where ℓ is the previously described intrinsic length scale. For our model, we found satisfactory results when $\ell = 0.6$ mm. (This translates to a η_c value of 0.1 for the SPH models shown in Figures 4 - 8, which use $h = 6$ mm.)

In our SPH simulations (just like in FEM), the width of a shear band is influenced by the discretization size (for SPH, the smoothing length, h). Thus it is reasonable to conclude that ℓ reflects the intrinsic width of a shear band in the experiments, and η_c quantifies a correction to the constitutive model that is necessary when h does not equal ℓ. This interpretation is further validated by the observation that the characteristic width of a shear band in sandbox analogue models directly varies with the sand grain size. Chevalier et al. (2012) report an average grain size of 0.5 mm. Given that ℓ was determined by completely independent means to be a very similar value, we postulate that ℓ is likely a reflection of the mean grain size. However, further investigation of this parameter is warranted in future work.

5.5 Scaling of analogue models

We now return to the scaling question posed in Section 3. Specifically, we are interested in whether it is safe to ignore the scaling of elastic parameters, as is customarily done in analogue sandbox

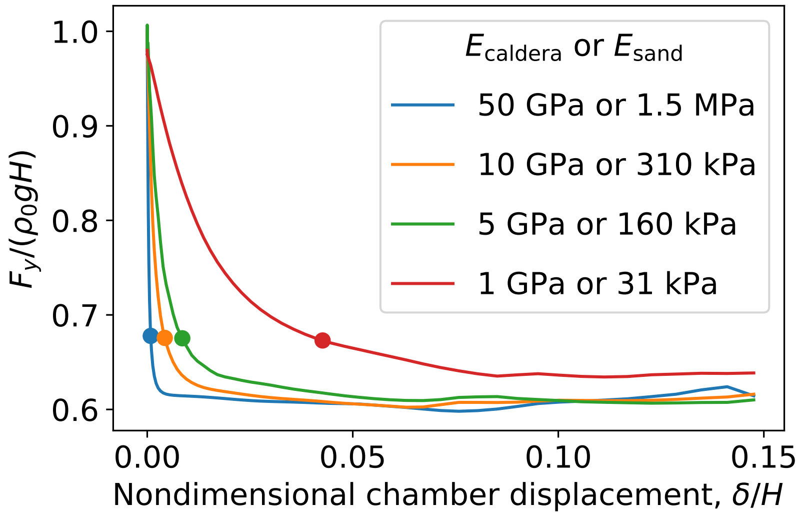

Figure 10. Non-dimensional vertical load exerted on the trapdoor as a function of non-dimensional displacement. Multiple values of the Young's modulus, E, are compared. Caldera scale model: $H = 1000$ m, $B = 2000$ m, $C = 3$ MPa, $\rho_0 = 2900$ kg/m^3. Sandbox scale model: $H = 0.05$ m, $B = 0.1$ m, $C = 93$ Pa, $\rho_0 = 1800$ kg/m^3. Both models: $\phi = \psi = 30°$, $\nu = 0.3$. Dots mark where the elastoplastic regime number Λ_{ep} as defined in Equation 4 equals 1.0. Results shown are from dimensional simulations using the caldera scale properties; results from dimensional simulations using sandbox scale properties give similar non-dimensional curves.

models. We therefore conducted a series of numerical tests to determine the model sensitivity to changing elastic moduli, using a constant (non-critical state) constitutive model with an associative flow rule (Figure 10) for simplicity. We first conducted tests at the caldera scale, setting c, ρ_0, H to be 3 MPa, 2900 kg/m^3, and 1000 m, respectively, as in Section 3. We further took B (trap-door width) to be 2000 m and ϕ to be 30°. Additionally, we varied the Young's modulus, E, over a wide range of values that are plausible for a jointed basaltic rock mass (Schultz, 1993), and measured the response of the model by plotting the vertical load exerted on the trapdoor as a function of trapdoor displacement.

Results from these numerical tests (Figure 10) suggest that for large trapdoor displacements, as plastic strains increase relative to elastic strains, the model responses will tend to converge and the scaling of E can be safely ignored. However, at smaller trapdoor displacements ($\delta/H < 0.05$ equating to $\delta = 50$ m in the caldera model shown in Figure 10), the choice of E does make a material difference to the model results. In this example, if the Young's modulus of the caldera rock is thought to be 1 GPa or less (in a heavily fractured rock mass, for example), E should be scaled in any analogue model, or the model will not provide valid results. For the example in Figure 10 and a caldera rock with Young's modulus of 1 GPa, this would demand use of a sand with a Young's modulus of 31 KPa. This presents a challenge for sandbox models, because it is likely difficult to obtain sands in this range of elastic moduli (Hardin, 1965).

Figure 10 further shows the utility of the non-dimensional elastoplastic regime number, Λ_{ep}, that we defined in Section 3. The results show that if Λ_{ep} is less than a factor of approximately 3, the elastic strains are sufficiently large to demand the scaling of elastic parameters.

5.6 Application to the 2018 eruption of Kīlauea

After successfully explaining the kinematics and forces of analogue models, we now turn our attention to real volcanic calderas. In the present work, we restrict our attention to the orientation of faults formed during the 2018 eruption of Kīlauea volcano (Figure 1). The 2018 collapse exploited pre-existing faults along its west and north sides. During the course of the three month long eruption, a new (at least at the surface) ring fracture system developed along the east side of the collapse. The 2018 collapse offers a uniquely rich data set detailing the process of caldera formation. Of particular interest is the high resolution seismic catalogue of precisely located earthquakes (Figure 1B; Shelly & Thelen, 2019). The most dominant feature of the catalogue is a clear, vertically-oriented distribution of events mainly associated with the surface trace of the eastern ring fault. This likely indicates that displacements were accommodated along a ring fault with a near-vertical dip to considerable depth ($\sim$2 km). This conclusion agrees with geodetic models which favor a vertical or near-vertical dip (Segall et al., 2019, 2020). Note that vertical faults are distinct from the observed kinematics of sandbox experiments, where ring faults are initially outward dipping.

Given this observation, our model can be used to make inferences about the constitutive behavior of the host rock at Kīlauea. We performed a series of tests using a simplified plane strain model geometry, and constitutive parameters judged appropriate for the Kīlauea caldera (Figure 11). We present results for both models with constitutive models with constant parameters (left and cen-

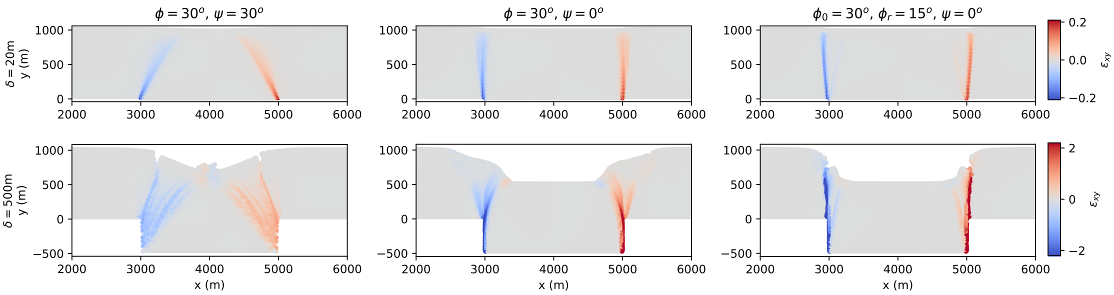

Figure 11. Caldera collapse simulation using parameters representative of Kīlauea volcano basalt. Left and center columns show results for models with constant material parameters; right column shows results for critical state model. $H = 1$ km, $B = 2$ km, $E = 10^{10}$ Pa, $\rho = 2900$ kg/m^3, $c = 3$ MPa, and $\Delta x = 20$ m. Note that models indicate some degree of rockslide into the caldera and forming of tension cracks. Tension cracks may be attributable to SPH numerical implementation.

ter columns, Figure 11) and employing a critical state constitutive law (right column, Figure 11). Because it is difficult to determine a natural length scale for shear bands in the Kīlauea context, we make the simple choice of setting $\eta_c = 1$ for our model employing the simplified critical state constitutive model (right column in Figure 11); this is an important source of uncertainty. As was the case for the analogue model simulations, a relatively low dilatancy is required for vertical ring faults to form. Alternatively, similar results could be obtained with a simplified critical state model with small η_c, such that the value of ψ would quickly drop to zero.

Note that we do not model several potentially important aspects of the 2018 Kīlauea caldera collapse. Among these are the preexisting presence of the Halema‘uma‘u crater and caldera ring faults. These factors clearly had an important role in the early phase of the collapse, but it is unlikely that they dominated the formation of the ring fault in the eastern sector. We also reserve an exhaustive exploration of the potential parameter space for future work. Varying parameters beyond ϕ and ψ would likely cause important effects; in a limited set of experiments we found that varying the cohesion could affect the near-surface expression of the model faults, where the influence of cohesion is non-negligible. However, varying cohesion does not influence the predicted fault dips at depth.

6 DISCUSSION

The non-dimensional parameter H/B, the chamber depth-to-width ratio, has been shown to be of central importance in determining the response of scaled analogue models and numerical experiments (Roche et al., 2000; Holohan et al., 2011). At low H/B the downgoing caldera block initially descends in a largely coherent manner along outwardly dipping reverse faults. At high H/B, on the other hand, the downgoing block may be broken into smaller parcels by multiple sets of reverse faults.

Our results provide a new lens through which to interpret this well established result. In sandbox analogue models, the faults which initially develop are outwardly dipping and originate at the boundary between the trapdoor at the adjacent bottom boundary of the experimental apparatus. Given the faults are outwardly dipping, it is clear that if they are allowed to extend upward indefinitely they will at some point intersect (Figure 2). In order for a caldera block to remain intact as it descends, therefore, the depth H must be sufficiently small relative the width B. Furthermore, the critical ratio of H/B at which the outward dipping faults intersect depends on the angle θ, the angle formed between the faults and vertical. It is straightforward to determine from the geometry of the problem that this critical value is

$$\frac{H}{B} = \frac{1}{2\tan\theta} = \frac{1}{2\tan\psi_0}, \tag{36}$$

where we have made the additional substitution that the intial fault orientation angle θ equals the initial angle of dilation ψ_0, as follows from our results.

In analogue experiments the critical value of H/B at which the transition in behavior occurs has been determined to be around $H/B \approx 1$ (Roche et al., 2000). This condition translates to a value of $\theta \approx 26^\circ$, which is very close to the initial value of the angle of dilation $\psi_0 = 30^\circ$ that we have determined necessary to fit the experimental data of Chevalier et al., 2012. Our results therefore support the conclusion the critical value of H/B at which a transition in behavior occurs is set by the angle ψ. Note that this conclusion signifies that experimental results based on H/B are fundamentally a reflection of the *material properties* of the caldera rock (or rock analogue) and should therefore be applied with appropriate discretion to the caldera scale problem.

A clear lesson from our numerical modeling is that physically-realistic constitutive models are required to understand caldera formation and the behavior of analogue models. These constitutive models must not only consider the yield condition, but also, importantly, must consider *post*-yield behavior. Given relatively large plastic strains, any simplification of post-yield behavior will likely lead to incorrect results. Indeed, our results suggest the assumption that the material properties are constant leads to results which cannot explain observations in analogue experiments (Figures 4 and 8).

Instead, our results highlight the critical state nature of sand. Both the kinematics (Figure 7) and observed loads (Figure 8) of the Chevalier et al. (2012) experiments can be explained with a simplified critical state constitutive model. Theoretical considerations bolster this conclusion; given a direction of motion vertically downward, the orientation of shear bands (relative to vertical) should be primarily controlled by the angle of dilation. This paper thus strongly supports the view that the critical state nature of sand cannot be ignored in analogue models when the orientations of shear bands change with displacement.

While using the simplified critical state constitutive model shows satisfactory results, it should be emphasized that this model likely would fail to capture certain known behaviors of sands, like the transition from dilative to contractive behavior or plastic yield in pure compression. More advanced models of critical state elastoplasticty offer approaches for modeling these behaviors (Roscoe & Burland, 1968; Jefferies, 1993). The Nor-Sand constitutive model, in particular, offers an attractive option for the present problem because it well captures the dilatant behavior of dense sands during shearing (Borja, 2013). In future work, we plan to implement Nor-Sand as a constitutive model in our SPH framework.

In this paper we argue that the orientation of shear bands θ should be primarily determined by ψ, the angle of dilation. While our models adequately capture the behavior of many analogue models where shear bands rotate to be vertical at the later stages of deformation (Ruch et al., 2012; Chevalier et al., 2012), an objection to our results may be raised based on the frequently observed development of inward dipping normal faults at the later stages of caldera development (Acocella, 2021). These inward dipping faults may be explained by a negative angle of dilation (not possible in our model), but are more likely a reflection of passive, secondary activity that initiates only after the initial downward movement of the caldera block. This behavior is fundamentally extensional (i.e., dilational), and should be within the scope of our constitutive model. We hope to capture this kind of activity in future simulations.

In addition to elastoplastic models, several alternative continuum constitutive models exist and have shown promise for the modeling of granular media (Forterre & Pouliquen, 2008). Visco-plastic models, which model the shearing of grains as a fluid-like process, have been shown to capture many aspects of granular flow (Jop et al., 2006; GDR MiDi, 2004). These models could be implemented in SPH without much difficulty, and we plan to test the behavior of these models in future work.

The development of an appropriate continuum constitutive model for sand is doubtlessly a difficult task. Unfortunately, the development of an appropriate continuum constitutive model for the large-scale deformation of rock in a caldera forming eruption is no easier task either. While this issue represents a significant source of uncertainty in any modeling effort, it is our belief that numerical models are uniquely well equipped to provide valuable insights in this context. Numerical models allow for rapid experimentation with multiple constitutive models, highlighting model responses which are attributable to the specifics of any constitutive model. Furthermore, numerical models allow for experimentation with factors that we strongly expect would influence the deformation of rock in the caldera formation context, such as the layering of host rock (Gudmundsson, 2007), which might be difficult to explore with scaled analogue models.

Our results also demonstrate the utility of a numerical model for constraining the appropriate scaling of analogue models (Section 3). While it is customary to ignore the elastic moduli in scaling analogue models (Norini & Acocella, 2011; Ruch et al., 2012), our results indicate that this assumption is perhaps less valid than previously thought (Figure 10). While the assumption that the elastic part of the problem is negligible is likely correct for many scaled models, it may not be correct for models with low shear modulus, small displacement, or deep magma chambers (Equation 4). Before neglecting the scaling of elastic moduli in analogue experiments, care should be taken to ensure that the expected plastic strains are indeed much larger than elastic strains at all phases of interest (not just the final state).

Ultimately, the goal of both analogue and numerical models is to generate insights about the nature of real caldera forming events. Our results clearly demonstrate that the orientation of caldera ring faults is strongly influenced by ψ, the angle of dilation. In our critical state model, ψ decreases with increasing plastic strain. We can therefore connect our results to previous research on the relationship between caldera geometry and caldera maturity, where previous authors have found that immature systems tend to have outward dipping faults while mature systems have more vertical faults (Ruch et al., 2012). Our results help explain this observation; as strain accumulates the angle of dilation decreases and faults tend towards the vertical.

In the case of Kīlauea, where nearly-vertical ring faults have been inferred (Segall et al., 2019, 2020; Shelly & Thelen, 2019), our results support the conclusion that the angle of dilation for the host rock must be small. It is known that plastic strain and increased confining pressure can decrease the angle of dilation for rocks (Zhao & Cai, 2010). At Kīlauea the confining stresses at the depth of the magma storage zone are likely in the range of 10-100 MPa, which should be sufficient to reduce the angle of dilation (Zhao & Cai, 2010). Additionally, it should be noted that the 2018 eruption of Kīlauea saw the enhancement of a previously-existing caldera; in this way the host rock must have already experienced considerable plastic deformation during its earlier development.

We emphasize that this paper stops far short of a full exploration of the wide diversity of calderas found in nature. Observations from Kīlauea have been interpreted to indicate caldera block displacement along relatively vertical faults. But other calderas seem to be bounded by a range of collapse geometries, from outward dipping ring faults to inward dipping or mixed. Our results prompt speculation about what leads to these distinct geometries. As discussed above, outward dipping faults might indicate immature systems with high dilation angles. Inward dipping faults could be an indication of a negative dilation angle (not possible in our current constitutive model), extensional tectonic stress, or be an indication of more complex behavior (such as multiple interacting sets of faults). However, we stress that the present work is primarily meant as a proofof-concept for the method; a deeper exploration of applications to real world calderas is reserved for future work.

There are several natural extensions to this work. Implementation of additional constitutive models specifically designed for rock would clearly be advantageous. We also hope to soon perform 3D simulations of caldera formation. While previous studies show largely consistent results for 2D and 3D models (Roche et al., 2000), a full 3D simulation will allow for studying of more complex stress fields which can influence caldera development (Cabaniss et al., 2018). Incorporation of additional physics, such as thermal or viscous effects, could also generate useful insights. Perhaps the greatest limitation of our current SPH model is the restriction to displacement boundary conditions. In future work, we hope to implement stress boundary conditions, allowing us to model a pressure boundary on a depleting magma reservoir and to study the effect of varying regional tectonic stress, a factor that has previously been shown to play an important role in caldera development (Holohan et al., 2005; Cabaniss et al., 2018; Gudmundsson, 2006).

7 CONCLUSION

- SPH, as a mesh-free continuum numerical method, offers a compelling option for numerical modeling of finite elastoplastic deformation of rock and granular material.
- The kinematics and load-displacement curves of the Chevalier et al. (2012) experiments strongly indicate critical state behavior of the sand used in those and other similar experiments.
- The orientation of shear bands in analogue caldera formation models is primarily controlled by the angle of dilation.
- Proper scaling of analogue models might require consideration of elastic moduli. Numerical methods, such as SPH, can help diagnose if this scaling is needed. Furthermore, proper scaling requires a complete understanding of the constitutive behavior of rock and sand.
- The inferred vertical orientation of the ring fault structure at Kīlauea implies the caldera host rock likely has low dilatancy.

ACKNOWLEDGMENTS

B.M. is supported by an NSF GRFP fellowship and the Stanford Graduate Fellowship. P.S. acknowledges support from NSF EAR-2040425.

DATA AVAILABILITY

`GEOSPH`, the code used to perform the numerical simulations reported in this paper, is publicly available at https://github.com/alomirhfn/GEOSPH.git

References

Acocella, V. (2007). Understanding caldera structure and development: An overview of analogue models compared to natural calderas. *Earth-Science Reviews*, *85*(3-4), 125–160.

Acocella, V. (2021). Calderas. In *Volcano-tectonic processes* (pp. 163–203). Springer.

Andersen, K. H., & Schjetne, K. (2013). Database of friction angles of sand and consolidation characteristics of sand, silt, and clay. *Journal of Geotechnical and Geoenvironmental Engineering*, *139*(7), 1140–1155.

Anderson, K. R., Johanson, I. A., Patrick, M. R., Gu, M., Segall, P., Poland, M. P., . . . Miklius, A. (2019). Magma reservoir failure and the onset of caldera collapse at kilauea volcano in 2018. *Science*, *366*(6470), eaaz1822. doi: 10.1126/science.aaz1822

Borja, R. I. (2013). *Plasticity: modeling and computation*. Springer.

Branney, M., & Acocella, V. (2015). Calderas. In *The encyclopedia of volcanoes* (pp. 299–315). Elsevier.

Bui, H. H., & Nguyen, G. D. (2021). Smoothed particle hydrodynamics (sph) and its applications in geomechanics: From solid fracture to granular behaviour and multiphase flows in porous media. *Computers and Geotechnics*, *138*, 104315.

Bui, H. H., Sako, K., & Fukagawa, R. (2006). Non-cohesion material flows in rotating drum: Smoothed particle hydrodynamics (sph) and discrete element method (dem). In *Proceedings* *of the 41st japan national conference on geotechnical engineering (jgs). jgs vol. 41* (pp. 1–2). JGS.

Cabaniss, H. E., Gregg, P. M., & Grosfils, E. B. (2018). The role of tectonic stress in triggering large silicic caldera eruptions. *Geophysical Research Letters*, *45*(9), 3889–3895.

Carmichael, R. S. (1982). *Handbook of physical properties of rocks*. CRC Press.

Cashman, K. V., & Giordano, G. (2014). Calderas and magma reservoirs. *Journal of Volcanology and Geothermal Research*, *288*, 28–45.

Chevalier, B., Combe, G., & Villard, P. (2012). Experimental and discrete element modeling studies of the trapdoor problem: influence of the macro-mechanical frictional parameters. *Acta Geotechnica*, *7*(1), 15–39.

Costa, Y. D., Zornberg, J. G., Bueno, B. S., & Costa, C. L. (2009). Failure mechanisms in sand over a deep active trapdoor. *Journal of Geotechnical and Geoenvironmental Engineering*, *135*(11), 1741–1753.

Cundall, P. A., & Strack, O. D. (1979). A discrete numerical model for granular assemblies. *geotechnique*, *29*(1), 47–65.

Davis, R. O., & Selvadurai, A. P. (2005). *Plasticity and geomechanics*. Cambridge university press.

del Castillo, E. M., Fávero Neto, A. H., & Borja, R. I. (2021a). A continuum meshfree method for sandbox-style numerical modeling of accretionary and doubly vergent wedges. *Journal of Structural Geology*, *153*, 104466.

del Castillo, E. M., Fávero Neto, A. H., & Borja, R. I. (2021b). Fault propagation and surface rupture in geologic materials with a meshfree continuum method. *Acta Geotechnica*, *16*(8), 2463–2486.

Fávero Neto, A. H. (2020). *A continuum lagrangian finite deformation computational framework for modeling granular flows*. Stanford University.

Fávero Neto, A. H., Askarinejad, A., Springman, S. M., & Borja, R. I. (2020). Simulation of debris flow on an instrumented test slope using an updated lagrangian continuum particle method. *Acta Geotechnica*, *15*(10), 2757–2777.

Fávero Neto, A. H., & Borja, R. I. (2018). Continuum hydrodynamics of dry granular flows employing multiplicative elastoplasticity. *Acta Geotechnica*, *13*(5), 1027–1040.

Forterre, Y., & Pouliquen, O. (2008). Flows of dense granular media. *Annu. Rev. Fluid Mech.*, *40*, 1–24.

Francis, T. (1974). A new interpretation of the 1968 fernandina caldera collapse and its implications for the mid-oceanic ridges. *Geophysical Journal International*, *39*(2), 301–318.

GDR MiDi. (2004). On dense granular flows. *The European Physical Journal E*, *14*, 341–365.

Geyer, A., & Martí, J. (2014). A short review of our current understanding of the development of ring faults during collapse caldera formation. *Frontiers in Earth Science*, *2*, 22.

Gingold, R. A., & Monaghan, J. J. (1977). Smoothed particle hydrodynamics: theory and application to non-spherical stars. *Monthly notices of the royal astronomical society*, *181*(3), 375–389.

Gray, J. P., & Monaghan, J. J. (2003). Caldera collapse and the generation of waves. *Geochemistry, Geophysics, Geosystems*, *4*(2).

Gray, J. P., & Monaghan, J. J. (2004). Numerical modelling of stress fields and fracture around magma chambers. *Journal of Volcanology and Geothermal Research*, *135*(3), 259–283.

Gregg, P., De Silva, S., Grosfils, E., & Parmigiani, J. (2012). Catastrophic caldera-forming eruptions: Thermomechanics and implications for eruption triggering and maximum caldera dimensions on earth. *Journal of Volcanology and Geothermal Research*, *241*, 1–12.

Gudmundsson, A. (2006). How local stresses control magma-chamber ruptures, dyke injections, and eruptions in composite volcanoes. *Earth-science reviews*, *79*(1-2), 1–31.

Gudmundsson, A. (2007). Conceptual and numerical models of ring-fault formation. *Journal of Volcanology and Geothermal Research*, *164*(3), 142–160.

Hardin, B. O. (1965). Dynamic versus static shear modulus for dry sand. *Materials research and standards*, *5*(5), 232–235.

Hardy, S. (2008). Structural evolution of calderas: Insights from two-dimensional discrete element simulations. *Geology*, *36*(12), 927–930.

Hildreth, W., & Mahood, G. A. (1986). Ring-fracture eruption of the bishop tuff. *Geological*

Society of America Bulletin, *97*(4), 396–403.

Holohan, E., Schöpfer, M., & Walsh, J. (2011). Mechanical and geometric controls on the structural evolution of pit crater and caldera subsidence. *Journal of Geophysical Research: Solid Earth*, *116*(B7).

Holohan, E., Schöpfer, M., & Walsh, J. (2015). Stress evolution during caldera collapse. *Earth and Planetary Science Letters*, *421*, 139–151.

Holohan, E., Troll, V. R., Walter, T. R., Münn, S., McDonnell, S., & Shipton, Z. (2005). Elliptical calderas in active tectonic settings: an experimental approach. *Journal of Volcanology and Geothermal Research*, *144*(1-4), 119–136.

Hubbert, M. K. (1937). Theory of scale models as applied to the study of geologic structures. *Bulletin of the Geological Society of America*, *48*(10), 1459–1520.

Iglesia, G. R., Einstein, H. H., & Whitman, R. V. (2014). Investigation of soil arching with centrifuge tests. *Journal of Geotechnical and Geoenvironmental engineering*, *140*(2), 04013005.

Jefferies, M. (1993). Nor-sand: a simle critical state model for sand. *Géotechnique*, *43*(1), 91–103.

Jellinek, A. M., & DePaolo, D. J. (2003). A model for the origin of large silicic magma chambers: precursors of caldera-forming eruptions. *Bulletin of Volcanology*, *65*(5), 363–381.

Jop, P., Forterre, Y., & Pouliquen, O. (2006). A constitutive law for dense granular flows. *Nature*, *441*(7094), 727–730.

Kabele, P., Žák, J., & Somr, M. (2017). Finite-element modeling of magma chamber–host rock interactions prior to caldera collapse. *Geophysical Journal International*, *209*(3), 1851–1865.

Lipman, P. W. (1997). Subsidence of ash-flow calderas: relation to caldera size and magma-chamber geometry. *Bulletin of volcanology*, *59*(3), 198–218.

Liu, M., & Liu, G. (2010). Smoothed particle hydrodynamics (sph): an overview and recent developments. *Archives of computational methods in engineering*, *17*(1), 25–76.

Lucy, L. B. (1977). A numerical approach to the testing of the fission hypothesis. *The Astronom-*

ical Journal, *82*, 1013–1024.

Monaghan, J. J., & Gingold, R. A. (1983). Shock simulation by the particle method sph. *Journal of computational physics*, *52*(2), 374–389.

Monaghan, J. J., & Lattanzio, J. C. (1991). A simulation of the collapse and fragmentation of cooling molecular clouds. *The Astrophysical Journal*, *375*, 177–189.

Neal, C. A., Brantley, S., Antolik, L., Babb, J., Burgess, M., Calles, K., … others (2019). The 2018 rift eruption and summit collapse of Kīlauea volcano. *Science*, *363*(6425), 367–374.

Norini, G., & Acocella, V. (2011). Analogue modeling of flank instability at mount etna: understanding the driving factors. *Journal of Geophysical Research: Solid Earth*, *116*(B7).

Panien, M., Schreurs, G., & Pfiffner, A. (2006). Mechanical behaviour of granular materials used in analogue modelling: insights from grain characterisation, ring-shear tests and analogue experiments. *Journal of Structural Geology*, *28*(9), 1710–1724.

Ramberg, H. (1981). *Gravity, deformation and the Earth's crust*. Academic press.

Roche, O., Druitt, T., & Merle, O. (2000). Experimental study of caldera formation. *Journal of Geophysical Research: Solid Earth*, *105*(B1), 395–416.

Roscoe, K., & Burland, J. (1968). On the generalized stress-strain behaviour of wet clay. In J. Heyman & F. Leckie (Eds.), *Engineering plasticity* (pp. 535–609). Cambridge University Press.

Roux, J.-N., & Combe, G. (2002). Quasistatic rheology and the origins of strain. *Comptes Rendus Physique*, *3*(2), 131–140.

Ruch, J., Acocella, V., Geshi, N., Nobile, A., & Corbi, F. (2012). Kinematic analysis of vertical collapse on volcanoes using experimental models time series. *Journal of Geophysical Research: Solid Earth*, *117*(B7).

Schultz, R. A. (1993). Brittle strength of basaltic rock masses with applications to venus. *Journal of Geophysical Research: Planets*, *98*(E6), 10883–10895.

Segall, P., Anderson, K. R., Johanson, I., & Miklius, A. (2019). Mechanics of inflationary deformation during caldera collapse: Evidence from the 2018 kīlauea eruption. *Geophysical Research Letters*, *46*(21), 11782–11789.

Segall, P., Anderson, K. R., Pulvirenti, F., Wang, T., & Johanson, I. (2020). Caldera collapse geometry revealed by near-field gps displacements at kīlauea volcano in 2018. *Geophysical Research Letters*, *47*(15), e2020GL088867.

Shelly, D. R., & Thelen, W. A. (2019). Anatomy of a caldera collapse: Kīlauea 2018 summit seismicity sequence in high resolution. *Geophysical Research Letters*, *46*(24), 14395–14403.

Smith, R. L., & Bailey, R. A. (1968). Resurgent cauldrons. *Geological Society of America Memoirs*, *116*, 613–662.

Terzaghi, K. (1936). Stress distribution in dry and in saturated sand above a yielding trap-door. In *Proceedings of international conference of soil mechanics* (Vol. 1, pp. 307–311). Harvard University.

Terzaghi, K. (1943). Arching in ideal soils. *Theoretical soil mechanics*, 66–76.

Violeau, D. (2012). *Fluid mechanics and the sph method*. Oxford University Press.

Wendland, H. (1995). Piecewise polynomial, positive definite and compactly supported radial functions of minimal degree. *Advances in Computational Mathematics*, *4*(1), 389–396.

Wood, D. M. (1990). *Soil behaviour and critical state soil mechanics*. Cambridge university press.

Zabala, F., & Alonso, E. (2011). Progressive failure of aznalcóllar dam using the material point method. *Géotechnique*, *61*(9), 795–808.

Zhao, X., & Cai, M. (2010). A mobilized dilation angle model for rocks. *International Journal of Rock Mechanics and Mining Sciences*, *47*(3), 368–384.

APPENDIX A: SPH IMPLEMENTATION DETAILS

An explicit stress-point integration algorithm is employed in SPH and in this paper. Based on the Jaumann stress rate (Eq. 22), the Cauchy stress rate tensor is updated over time as

$$\boldsymbol{\sigma}_{n+1} = \boldsymbol{\sigma}_n + \Delta t \boldsymbol{C}_n^{\mathrm{ep}} : \boldsymbol{d}_n + \boldsymbol{R} \cdot \boldsymbol{\sigma}_n - \boldsymbol{\sigma}_n \cdot \boldsymbol{R}, \qquad \boldsymbol{R} = \Delta t \boldsymbol{\omega}_n \,. \tag{A.1}$$

At each time step, the position, velocity, mass density, stress, and deformation are updated for each particle in the domain. Any explicit time integration scheme can be used, but in this paper, we used a variation of the explicit forward Euler method that has optimum conservation characteristics as shown in Violeau (2012). In general, given a field variable $f(\boldsymbol{x})$ whose value is known at step n, corresponding to simulation time t_n, the updated value of that variable at step $n+1$, with corresponding time t_{n+1}, is given by

$$f(\boldsymbol{x})_{n+1} = f(\boldsymbol{x})_n + \dot{f}(\boldsymbol{x})_n \Delta t \,, \tag{A.2}$$

where $\dot{f}$ is the material time derivative of the variable, and $\Delta t = t_{n+1} - t_n$.

Hence, at the end of each time step, the positions, velocities, mass densities, and deformation are updated as follows,

$$\boldsymbol{v}_{n+1} = \boldsymbol{v}_n + \boldsymbol{a}_n \Delta t \,, \tag{A.3}$$

$$\boldsymbol{x}_{n+1} = \boldsymbol{x}_n + \boldsymbol{v}_{n+1} \Delta t \,, \tag{A.4}$$

$$\boldsymbol{\rho}_{n+1} = \boldsymbol{\rho}_n + \dot{\boldsymbol{\rho}}_n \Delta t \,, \tag{A.5}$$

$$\boldsymbol{\varepsilon}_{n+1} = \boldsymbol{\varepsilon}_n + \boldsymbol{d}_n \Delta t \,. \tag{A.6}$$

Note that the first two updates have to be performed in the order presented above for optimum conservation to be achieved. Furthermore, the material time derivative of the mass density is given by Equation 20, and the update equation for the deformation tensor can be performed for the elastic and plastic components as well, making use of the additive split of the deformation gradient tensor, $\boldsymbol{d} = \boldsymbol{d}^{\mathrm{e}} + \boldsymbol{d}^{\mathrm{p}}$. For further details on the update of deformations see Fávero Neto (2020).

In the previous update equations, the time step Δt has to satisfy the CFL conditions (Fávero Neto & Borja, 2018) in order to render the update stable. In this paper, the CFL condition is represented by

$$\Delta t \leq a\frac{h}{c_s}\,, \tag{A.7}$$

where a is a coefficient chosen to be 0.1, and $c_s = \sqrt{E/\rho}$ is the numerical speed of sound of the material with Young's modulus E.

Another important numerical aspect to observe is that due to its dynamic nature, SPH (like other dynamic methods) requires some level of dampening of elastic shock waves (artificial viscosity) in the domain, which otherwise may lead to loss of stability and accuracy of the solution. In this paper, we use the well-established artificial viscosity term proposed by Monaghan and Gingold (1983). The artificial viscosity term is added to the balance of linear momentum, Equation 19 as follows

$$\langle \boldsymbol{a} \rangle_i = \sum_{j=1}^{N} m_j \left(\frac{\boldsymbol{\sigma}_i + \boldsymbol{\sigma}_j}{\rho_i \rho_j} + \Pi_{ij}\mathbf{1} \right) \cdot \nabla \otimes W_{ij} + \boldsymbol{g}_i\,, \tag{A.8}$$

where

$$\Pi_{ij} = \begin{cases} \dfrac{\alpha_\pi c_{s,ij}\Phi_{ij} - \beta_\pi \Phi_{ij}^2}{\rho_{ij}}, & \text{for } \boldsymbol{v}_{ij} \cdot \boldsymbol{x}_{ij} < 0\,, \\ 0, & \text{for } \boldsymbol{v}_{ij} \cdot \boldsymbol{x}_{ij} \geq 0\,, \end{cases} \tag{A.9}$$

with

$$\Phi_{ij} = \frac{h_{ij}\boldsymbol{v}_{ij} \cdot \boldsymbol{x}_{ij}}{|\boldsymbol{x}_{ij}|^2 + \eta^2}\,, \tag{A.10}$$

where $c_{s,ij} = (c_{s,i} + c_{s,j})/2$, $\rho_{ij} = (\rho_i + \rho_j)/2$, $h_{ij} = (h_i + h_j)/2$, $\boldsymbol{x}_{ij} = \boldsymbol{x}_i - \boldsymbol{x}_j$, $\boldsymbol{v}_{ij} = \boldsymbol{v}_i - \boldsymbol{v}_j$, and $\eta = 0.01 h_{ij}$. The coefficients α_π and β_π are constants between 0 and 1.0, and in this paper were chosen to be $\alpha_\pi = 0.4$ and $\beta_\pi = 0$.

As mentioned previously, the assumption that the kernel domain is far from the problem domain boundaries is not true for particles near or at the problem boundary. For those particles, the kernel gradient will not guarantee first order consistency, which is necessary for convergence and accuracy of the method. Hence, a kernel gradient correction is required as described in Bui and Nguyen (2021). The corrected kernel gradient is given by

$$\tilde{\nabla} \otimes W_{ij} = \boldsymbol{L}_i \cdot \nabla \otimes W_{ij}\,, \tag{A.11}$$

where

$$\boldsymbol{L}_i = \left[\sum_{j=1}^{N} \frac{m_j}{\rho_j} \left(\boldsymbol{x}_j - \boldsymbol{x}_i\right) \otimes \left(\nabla \otimes W_{ij}\right)\right]^{-1} . \tag{A.12}$$

The corrected kernel gradient of Equation A.11 should be used in place of $\nabla \otimes W_{ij}$ in all applicable SPH operators, except in the balance of linear momentum, Equation 19 to enforce conservation (Bui & Nguyen, 2021).

Finally, it is important to provide a brief discussion on how to enforce Dirichlet boundary conditions (prescribed displacement) in SPH. The simplest way to enforce rigid boundary conditions like walls or moving rigid bodies interacting with the geotechnical/geological materials is through the introduction of so-called dummy boundary particles. These particles are placed at a distance $0.5\Delta x$ from the actual boundary line and outside the domain. Usually three to four layers of particles are sufficient. These particles neither move (or move with prescribed displacements) nor have their properties such as mass density and mass updated, with the exception of their stress tensor. However, they help enforce no-penetration and no-slip boundary conditions by entering the calculations of the deformation rate tensor and in the balance of linear momentum.

To update the stress tensor of the dummy particles, the stress of the deformable material is extrapolated to the dummy particles using the following expression

$$\boldsymbol{\sigma}_b = \left(\frac{1}{\sum\limits_{d=1}^{N_b} \frac{m_d}{\rho_d} W_{bd}}\right) \sum_{d=1}^{N_b} \frac{m_d}{\rho_d} \boldsymbol{\sigma}_d W_{bd} \, , \tag{A.13}$$

where subscripts b and d refer to the boundary particles and deformable material particles respectively, and N_b is the number of deformable particles that are neighbors of the boundary particle. For more information about the boundary formulation presented here the reader is referred to Bui and Nguyen (2021).